

POLITECNICO DI TORINO
McMASTER UNIVERSITY



Department of Mechanical and Aerospace Engineering

Master of Science in Mechanical Engineering

Master's Thesis

**RESIDUAL STRESS PREDICTION OF ADDITIVE
MANUFACTURED ELECTRIC MOTOR CORES
USING FINITE ELEMENT ANALYSIS**

Supervisors:

Belingardi Giovanni

Elbestawi Mo

Mostafa Yakout Mohamed

Candidate:

Miriam Galerati

December 2020

To Sachi

Abstract

This thesis work aims to investigate the possibility to use selective laser melting (SLM) to produce electric cores for a traction electric motor. SLM is a powder bed based additive manufacturing (AM) technique that guarantees relative structural density of the build part $> 99\%$. This is one of the reasons why SLM is among the most interesting processes to research on in the field of electric motors produced by AM. However, this technique is also characterized by significant residual stresses because of the high and repeated temperature gradients during the construction making it similar to a laser welding process. The prediction of residual stress is conducted in this study by performing a thermal-to-structural Finite Element Analysis (FEA) on a commercial software for additive processes (ANSYS Workbench) with one material available in its library (316 stainless steel). An initial check of the accuracy of the model is conducted by performing a convergence analysis, with a threshold of 3% of change.

The outcome of this part of the work is extremely encouraging from both a mathematical and physical standpoint. Indeed, the converged results show that the model is mathematically well-posed; while the physical discussion of the stresses highlights the accordance of the results with the theories explaining residual stress in SLM parts.

A second part of the study consists in investigating the possibility of mitigating residual stress by changing the energy density of the process. At first, the parameters in the simulation are set to be consistent with previous research aiming at optimizing the process inputs to get a full dense part. The process parameters are subsequently changed to get different values of energy density. It is shown that the residual stress experiences a significant reduction only with very small values on energy density, that would most probably result in non-full dense part.

The last section of this study involves a mechanical topological optimization. By trial and error, an optimized geometry is proposed in order to reduce the mass by keeping the same total deflection and residual stress in the rotor.

Contents

1	Introduction	17
2	Conventional electric motors	21
2.1	Electrical vehicles (EVs)	21
2.1.1	EV composition	23
2.1.2	Hybrid electrical vehicles HEVs	24
2.1.3	Some technical hurdles to EVs/HEVs widespread	26
2.2	Conventional production of electric motors	26
2.3	Working principle of an electric motor	28
3	Soft magnetic alloys	31
3.1	Applications of soft magnetic materials	33
3.1.1	Eddy-currents	33
3.2	Common soft magnetic materials	34
3.2.1	Electrical steel	34
3.2.2	Fe-Ni Alloys	35
3.2.3	Fe-Co Alloys	35
3.2.4	Soft magnetic composites	36
3.2.5	Soft ferrites	36
4	Additive Manufacturing processes	37
4.1	AM potential and challenges	39
4.2	Classification of AM processes	41
4.3	AM defects	42
4.4	SLM	45
4.4.1	SLM process parameters	47
4.4.2	Residual stress in SLM produced parts	49
5	Traction electric motors produced by AM	53

6	Finite Element Analysis (FEA) of rotor	57
6.1	Geometry	58
6.2	Material properties and build settings	59
6.2.1	Process parameters	63
6.3	Transient thermal simulation	64
6.4	Static structural analysis	64
7	Results of FEA	67
7.1	Check of accuracy of the model	72
7.2	Sensitivity analysis: energy density	73
8	Topological optimization	79
8.1	Settings of the topological optimization	80
8.2	Optimized proposed design	81
9	Conclusions and final remarks	87

List of Figures

2.1	<i>EV subsystems [55]</i>	23
2.2	<i>Working principle of parallel hybrid and series hybrid</i>	24
2.3	<i>Energy and power demands on batteries for different HEVs [38]</i>	25
2.4	<i>Weight of three sources of energy for 0.5 kWh of energy</i>	26
2.5	<i>Overall process for traction electric motor production</i>	27
2.6	<i>Effects of stamping process on the electric cores</i>	28
2.7	<i>Typical geometry of a PMDC motor [40]</i>	29
2.8	<i>Induction motor components [39]</i>	30
3.1	<i>Hysteretic curve: difference between hard and soft magnets [56]</i>	32
4.1	<i>Principle of additive manufacturing [53]</i>	38
4.2	<i>Support material during AM: supports for printability (on the left) and supports for balance (on the right). Figure adapted from [54]</i>	39
4.3	<i>Cost per piece vs geometric complexity in AM</i>	40
4.4	<i>Classification of additive manufacturing techniques</i>	41
4.5	<i>Working principles of PBF and DED processes [49]</i>	42
4.6	<i>Comparison between additive techniques and traditional techniques</i>	43
4.7	<i>Conceptual representation of the stair stepping effect</i>	44
4.8	<i>Cracks (on the left) and delamination (on the right) of AM parts. (Illustration adapted from [49])</i>	45
4.9	<i>Concept of SLM</i>	46
4.10	<i>Illustration of SLM process parameters [32]</i>	47
4.11	<i>Illustration of keyhole formation [19]</i>	48
4.12	<i>Explanation of the temperature gradient mechanism [57]</i>	49
4.13	<i>Illustration of the cool-down mechanism [56]</i>	50
4.14	<i>Types of residual stresses [56]</i>	51

5.1	<i>Illustration of the pauses during one-sequence build of an electric motor from [34]</i>	54
5.2	<i>Results of a 3D-printed 3-phase brushless DC motor [34]</i>	54
5.3	<i>Illustration of an SLM-produced rotor [35]</i>	55
5.4	<i>Illustration of SLM-produced stators [1] made of two different materials</i>	55
6.1	<i>Geometry (on the left) and orientation (on the right) of the rotor</i>	58
6.2	<i>Geometry and orientation of build plate base and rotor</i>	59
6.3	<i>Maraging steel properties for the build plate</i>	60
6.4	<i>Density curve for 316 stainless steel from ANSYS Engineering Data</i>	61
6.5	<i>Coupled transient thermal and structural analysis in ANSYS Workbench</i>	62
6.6	<i>Cartesian mesh of the rotor</i>	62
6.7	<i>Process parameters</i>	63
6.8	<i>Boundary condition for transient thermal analysis (on the left) and static structural analysis (on the right)</i>	64
6.9	<i>Step of thermal and structural analysis</i>	65
7.1	<i>Equivalent Stress; max location</i>	67
7.2	<i>Equivalent Stress; min location</i>	67
7.3	<i>Maximum principal stress; location of the maximum value</i>	68
7.4	<i>Maximum principal stress; location of the minimum value</i>	68
7.5	<i>Minimum Principal Stress</i>	68
7.6	<i>Total deflection (scale 10)</i>	69
7.7	<i>Vertical line in the rotor volume</i>	70
7.8	<i>Maximum Principal Stress as a function of z-coordinate (building direction)</i>	70
7.9	<i>Minimum Principal Stress as a function of z-coordinate</i>	71
7.10	<i>Equivalent Stress as a function of z-coordinate</i>	71
7.11	<i>Convergence analysis: equivalent stress versus mesh size</i>	73
7.12	<i>Sensitivity analysis: equivalent stress versus energy density</i>	76
8.1	<i>Workflow for topological optimization of AM parts in ANSYS</i>	80
8.2	<i>Geometrical settings of the topological optimization analysis in ANSYS</i>	80
8.3	<i>Optimized geometry with 52% of mass retained</i>	81
8.4	<i>Optimized geometry with 70% of mass retained</i>	82
8.5	<i>Optimized geometry with 60% of mass retained</i>	82
8.6	<i>Design with 70% mass retained. Total deflection - true scale</i>	83

8.7	<i>Design with 70% mass retained. Total deflection - scale 16 .</i>	83
8.8	<i>Design with 70% mass retained. Equivalent stress - true scale</i>	83
8.9	<i>Design with 60% mass retained. Total deflection - true scale</i>	84
8.10	<i>Design with 60% mass retained. Total deflection - scale 16 .</i>	84
8.11	<i>Design with 60% mass retained. Equivalent stress - true scale</i>	84
9.1	<i>Example of multimaterial design with alternating vertical sheets of electrical steel and magnetic insulator [20]</i>	88

List of Tables

2.1	<i>Classification and features of EVs</i>	22
4.1	<i>AM part common defects and inspection methods</i>	42
6.1	<i>Typical maraging steel compositions</i>	59
6.2	<i>Typical 316 stainless steel compositions</i>	60
7.1	<i>Intermediate results of the convergence analysis</i>	72
7.2	<i>Relative change for convergence check</i>	72
7.3	<i>Process parameters in the reference combination</i>	74
7.4	<i>Results of process parameter tuning mitigation strategy</i>	75
8.1	<i>Retained mass, total deflection and equivalent stress during topological optimization</i>	85

Chapter 1

Introduction

In the recent years, additive manufacturing (AM) has undergone a great evolution, developing from a prototyping technology to a promising production alternative in disparate sectors. A deep understanding of the processes and how their parameters influence the result could guarantee not only the same properties as a conventionally produced product [17], but also to benefit from the unique advantages of AM, such as topological optimization and quasi-infinite freedom in design. Using lightweight components is a major target in an increasing number of industries, specifically automotive and aerospace in which every kilogram saved in design has a great impact on performances, costs (material, fuel,...), and environmental sustainability. An example of that is the field of power electrical machines, where most of the companies are trying to produce such a lightweight design that cannot be obtained by conventional technologies [20]. AM processes can be an option to reach this goal with innovative designs, improved magnetic and thermal properties [1] and reduced production times because of the absence of traditional tooling and, in turn, reduced production costs. Even though AM may successfully respect some requirements of electrical motors, other challenges need to be addressed before AM becomes a reliable technology for electrical machine applications.

A recent study [1] has investigated the fabrication of motor stators by selective laser melting (SLM) process in three different soft magnetic materials: stainless steel 430L, Fe50Ni, and Fe6Si. A first part of the study was aimed to find the optimum range for the parameters of the process. Density measurement was used to check the result. A dense component is characterized by minimal void formation and vaporization of alloying elements, which are common SLM defects. In this preparatory analysis, the optimum set of parameters was found for all the materials by printing a cube with an

edge length of 10 mm. However, since Fe6Si showed a brittle behavior, only stainless steel 430L and Fe50Ni were used in the second part of the study. The latter two materials were used to additively fabricate motor stators. Their electromagnetic performances were tested and then compared with those of a conventionally produced motor, with the following results: the electrical resistance was found to be in line with the reference motor, while the inductance was lower in SLM-printed motors. Since the tested stators had no isolators, producing them with a multi-material SLM process is a future work recommended by the authors of [1], as well as the investigation of post-processing and finishing treatments that was not included in the study.

The need for more electrification and the fast advance in AM inspire this thesis work, while the previous research on the feasibility of AM to produce electric machines constitute its starting point. The purpose of the study is to contribute to the development of this scientific-technological field with an experimental work on residual stress of a rotor produced by SLM. Indeed, residual stress is one of the major issues of SLM (because of fast and repeated heating and cooling) and the resulting distortion can also make the part unacceptable.

The work consists of four main sections, as detailed hereafter. The purpose of the initial chapters is to give an overview of the theoretical background with a focus on conventionally produced electric motors (*Chapter 2*), soft magnetic alloys (*Chapter 3*) and additive manufacturing processes (*Chapter 4*). This review not only illustrates the theoretical foundation of the work but also provides the state of the art of electric motors fabricated by AM, the potential of this topic and its current hurdles. In particular, *Chapter 5* demonstrates the great commercial interest in producing electric machines by AM. However, some issues still require attention before AM can be an alternative to the conventional way of producing electric motors.

In the second section, Finite Element Analysis is applied to predict the residual stress in a rotor. The analysis is run on the academic software ANSYS Workbench 2020 R2. The outcomes of the simulation are compared with the theories explaining the mechanisms of formation of residual stress in SLM parts, namely temperature gradient mechanism (TGM) and cool-down mechanism. A convergence analysis is run as first check of the accuracy of the model. It is performed by manually refining the mesh of the build part with a target threshold of 3% to interrupt the iterations. *Chapter 6* describes the procedure, geometry and assumptions of the analysis. The results and their discussion are illustrated in *Chapter 7*.

The simulation described above is run by setting the process parameters accordingly to the values found in the literature for similar materials. This choice should guarantee that the build part is full-dense. In the third section of this study the values of the process parameters are modified to conduct a sensitivity analysis. Five different combinations of parameters are tested to assess the effectiveness of varying the energy density in reducing residual stress.

The last section of the work (*Chapter 8*) consists in a topological optimization of the rotor to show how the production of electric motors can benefit from the quasi-infinite freedom in design that characterizes AM processes. The optimization is based on the mechanical loads involved in the additive production of the rotor, while the electromagnetic considerations are not part of this work.

A final chapter highlights the contributions of this work to the promising field of electric motors produced by AM. Recommendations for future works are also provided in *Chapter 9*.

Chapter 2

Conventional electric motors

After the first commercial hybrid electric vehicle (HEV) was sold at the end of 90's, the market of electrical machines for automotive applications has encountered a great growth for both fully electrical vehicles (PEVs) and HEVs [22]. A strong impetus to the development of these technologies is the ever increasing concern of many governments for the issues of climate change. The global discussion on the negative impact of man's activities has never stopped since the early 21st century. Not only does fossil fuel burning results in severe air pollution, but also the depletion of non-renewable resources is proceeding frighteningly fast, with some resources expected to be totally exploited by the end of this century.

Electrification in the transportation sector would address both the roadside emission issues as well as the need for technologies that rely on renewable energy sources.

The purpose of this Chapter is to present a brief overview of the electrical vehicles and of the traditional manufacturing process of their electric motors.

2.1 Electrical vehicles (EVs)

EV are road vehicles in which at least a portion of the propulsion is guaranteed by an electrical system. EVs can be divided into [22]:

- pure electric vehicles (PEVs), where no internal combustion engine (ICE) is present and thus, the battery is the only energy source and it can be recharged from an external electric power source. Zero emission results from driving on PEVs;
- hybrid electric vehicles (HEVs), in which both ICE and battery provide the propulsion. Low emissions are associated to their use. Dis-

parate types of HEVs exist - namely parallel hybrid, series hybrid, power split hybrid - as well as many subcategories;

- fuel cell electric vehicles (FCEVs): a FCEV can be seen as an hybrid vehicle with fuel cell instead of ICE. In a FCEV, the main power supplier is an electrochemical device that relays upon a chemical reaction to generate electrical energy.

PEVs and FCEVs are highly attractive for their zero roadside emission. However, the overall emissions should be taken into account: the manufacturing process and the chemical contamination related to the production of fuel cells and batteries [41] should be considered when comparing these systems to the traditional ones. Finally, the energy source for electricity is another key factor to determine the ultimate advantage of using an EV/HEV: renewable energy sources results in the best ecological benefits. On the contrary, if the main energy source of the country is coal power, the CO_2 impact may be even larger than an ICE. The characteristics of the aforementioned EV types are listed in Table 2.1, from reference [22].

Types of EV	PEV	HEV	FCEV
Energy source	(i) Battery	(i) Battery/ultracapacitor (ii) Internal combustion engines	(i) Fuel cells
Propulsion technique	(i) Electric motor drives	(i) Electric motor drives (ii) Internal combustion engines	(i) Electric motor drives
Characteristics and feature	(i) Zero emission (ii) Short driving range (iii) Higher initial costs	(i) Low emission (ii) Longer range (iii) Complex	(i) Zero emission (ii) Highest initial costs (iii) Medium driving range
Major techniques	(i) Electric motor control (ii) Battery management (iii) Charging device	(i) Electric motor control (ii) Battery management (iii) Managing multiple energy sources and optimal system efficiency (iv) Components sizing	(i) Fuel processor (ii) Fueling system (iii) Fuel cell cost
Regenerative braking	(i) Yes	(i) Yes	(i) Yes

Table 2.1: *Classification and features of EVs*

2.1.1 EV composition

The EV composition can be described as consisting of three main subsystems [55]:

- electric propulsion subsystem: the electric motor falls into this subsystem, together with electronic controller, power converter, mechanical transmissions and driving wheels;
- energy source subsystem: it comprises the energy source together with its management unit and refuelling unit;
- auxiliary subsystem: it involves some auxiliary units, namely temperature control unit, power steering unit and auxiliary power supply.

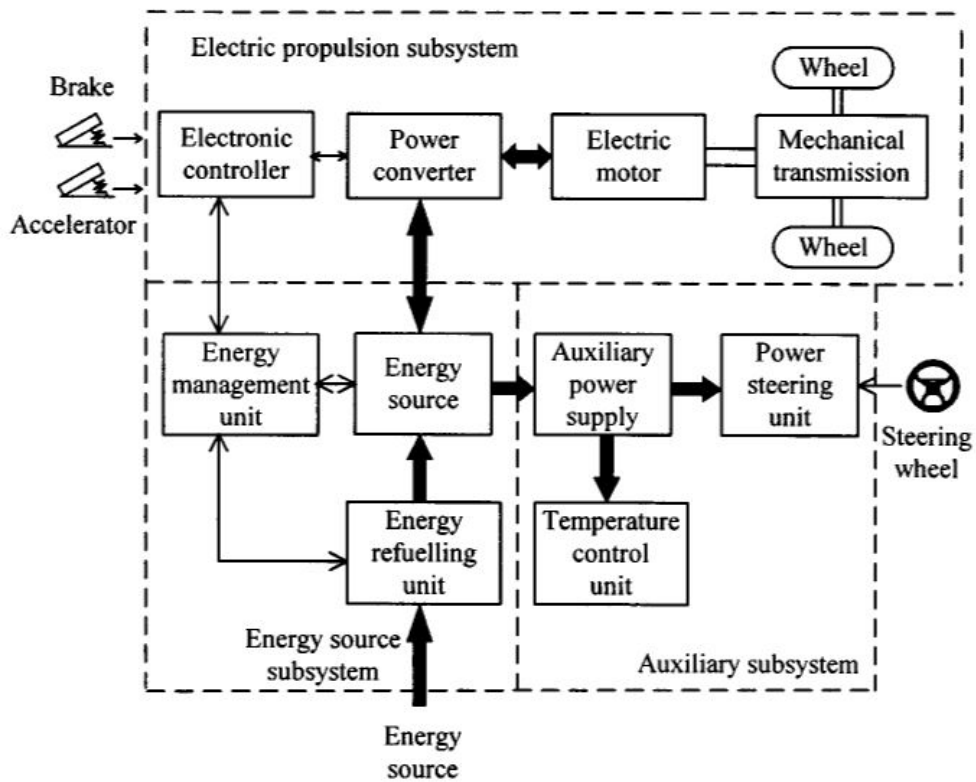


Figure 2.1: *EV subsystems* [55]

Figure 2.1 from [55] illustrates the three subsystems and the mutual connections: the mechanical, electrical and control links are represented by a double line, a thick line and a thin line, respectively. The arrows show the direction of the control information or power flow.

2.1.2 Hybrid electrical vehicles HEVs

HEVs are characterized by the presence of both an ICE and an electric motor. They can be classified on the basis of both the drivetrain arrangement and the involvement of the electric motor.

Figure 2.2 illustrates the working principles of both the parallel hybrid and series hybrid, showing the different drivetrain arrangements: in the series hybrid configuration, the electric motor powers the wheels and the ICE acts solely as a generator; the parallel hybrid is characterized by mechanical connection between the drivetrain and both the ICE and electric motor. In the latter configuration, the electric battery's role is to support the ICE, while in the series HEV it constitutes the main power source, meaning that a large capacity battery is required.

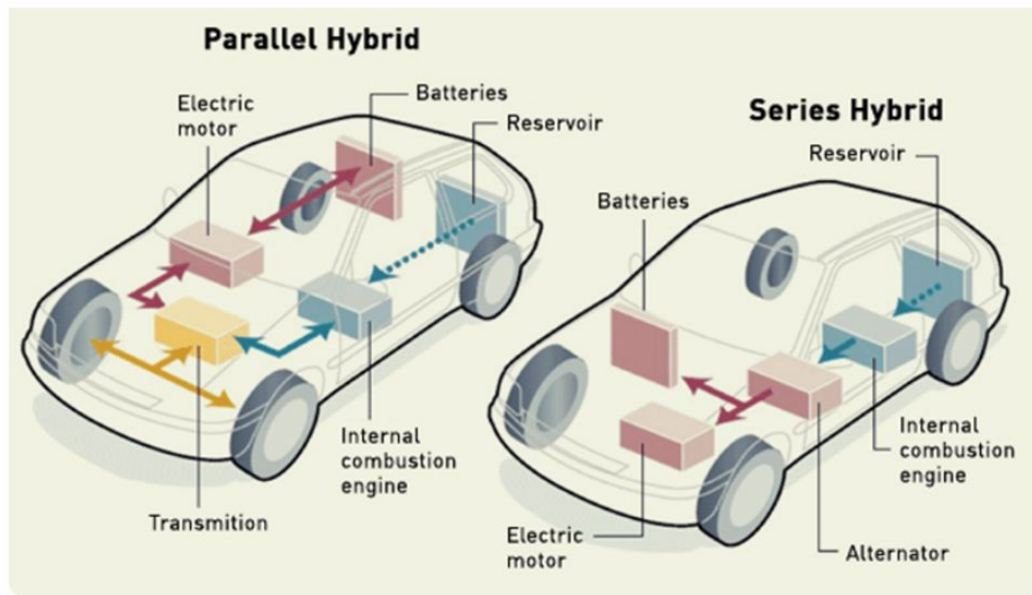


Figure 2.2: Working principle of parallel hybrid and series hybrid

Depending on the involvement of the electric motor, HEVs can be divided into:

- Full HEVs, with a fuel consumption reduction of about 40 % [37]. The electric system is used mainly when the ICE is operating with low efficiency. The battery is partially discharged when the electric motor is in function, while recharging is guaranteed by both ICE and regenerative braking;

- Mild HEVs, with fuel consumption savings of 15-20%. In this case, the electric system functions mainly for starting the vehicle and during acceleration. Regenerative charging of the battery happens during decelerations and brakings.
- Micro HEVs, with fuel consumption reduced by less than 10% (in urban driving mode). This configuration is characterized by the start-stop system: the engine is turned off during car stops and the electric system supplies energy for all the accessories. Micro HEVs are not considered hybrid electric anymore since no continuous power is supplied by the electric system and they are referred as *smooth starters* rather than e-machines.
- Plug-in HEVs, with both on-board regenerative charging and external source charging allowable. In this case, the ICE acts as a backup power source when the battery is exhausted.

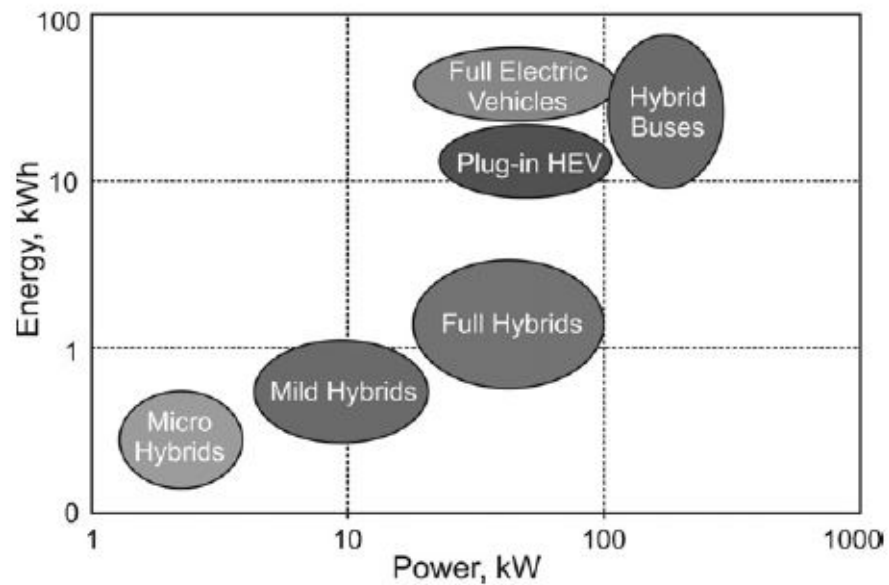


Figure 2.3: *Energy and power demands on batteries for different HEVs [38]*

2.1.3 Some technical hurdles to EVs/HEVs widespread

The advantages of EVs in terms of local emissions are indisputable and so is the urgency of more sustainable means of transport. However, some hurdles still need to be overcome for EVs to be an alternative to ICE vehicles. Limited range of EVs, their high cost and shorter lifetime compared to conventional propulsion systems are still limiting their widespread. Increase in charging infrastructures and standardization of size and location of the battery should also be considered for practical implementation of this technology [41]. From a mechanical standpoint, packaging and weight are two main topics to take into account when designing EV propulsion configurations: Figure 2.4 from source [23] explains why space and weight are problematic when it comes to EVs.



Figure 2.4: *Weight of three sources of energy for 0.5 kWh of energy*

2.2 Conventional production of electric motors

One major component of an electric or hybrid powertrain is the electric motor, whose objective is the conversion of the electric energy stored in the battery into mechanical energy to move the rotor and the shaft coupled to it. During braking, an electric motor can act as a generator, recovering the mechanical energy that would be lost as heat and friction by converting it into electric energy. The driving force that allows an electric motor to

operate comes from the interaction between a magnetic field and the electric current in a wire winding.

The main components of a traction electric motor are:

- stator: this is the stationary part and it usually carries either windings or permanent magnets; it consists of thin metal sheets in order to reduce losses happening in solid cores.
- rotor: this is the moving part that allows the shaft to spin. The rotor usually carries currents through the conductors laid into it. The torque that makes the shaft rotate comes from the interaction between those currents and the magnetic field of the stator. The rotor is typically located inside the stator, but the opposite configuration also exists: in that case, the motor is defined inside out electric motor.

According to the conventional process, the motor and the stator are fabricated separately, but with some similar steps. An overview of the manufacturing process is shown in Figure 2.5 from [30].



Figure 2.5: Overall process for traction electric motor production

As illustrated in the scheme, both the stator and the rotor need the lamination stamping and stacking, as well as machining, coating and testing. The process starts with the cold-rolling of silicon-iron (Fe-Si) to the desired thickness. The application of insulative materials on the sheets prevents eddy currents between sheets and, thus, coating is performed before the stamping process. Then the cores are obtained by stacking and fixing the sheets. Final post-machining and heat treating are used to correct the burrs and relieve the stress introduced by the stamping process [29]. The consequences of the stamping process in terms of stress are shown in Figure 2.6 from [31].

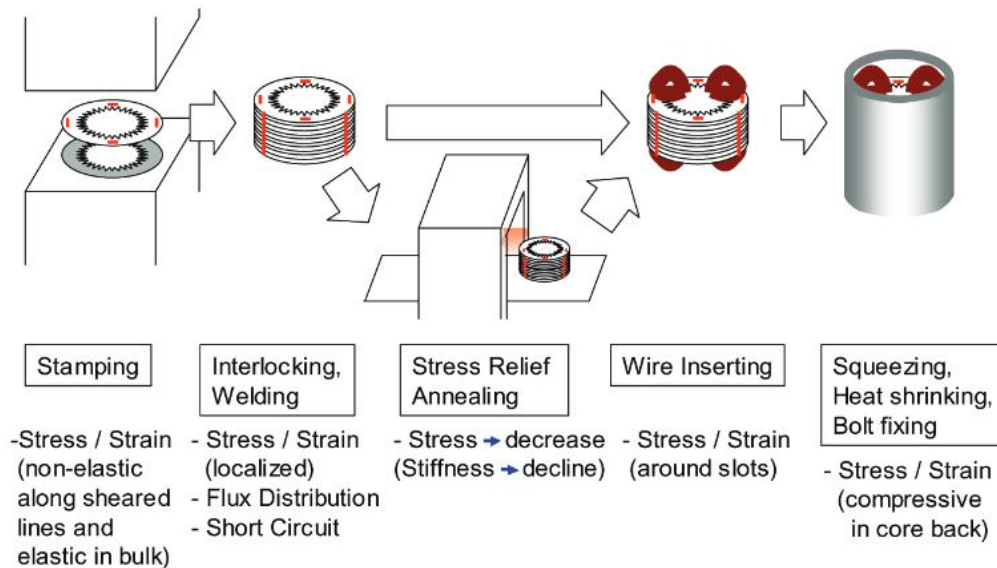


Figure 2.6: *Effects of stamping process on the electric cores*

2.3 Working principle of an electric motor

If a conductor with a current is placed into a magnetic field (perpendicular to the current), a force will act on it. If the conductor is bent into a frame so that there are two sides of the frame that are at right angle to the magnetic field, then the two sides will experience oppositely directed forces (with same magnitude). These opposite but equal forces create the moment making the conductor rotate. The magnetic field can be generated by either

permanent magnets or electromagnets that are typically a wire wound on a core. In this latter case, the magnetic field will be the result of Faraday's law of induction: the current in the conductors (for example in the rotor) will induce a current in the windings (in the stator), which in turn will create a magnetic field [35].

This working principle applies to all types of electric motor. At least a dozen different categories of electric motors exist, but a major classification between alternating current (AC) and direct current (DC). Brushed and brushless motors are two subcategories of DC motor, with Permanent Magnet DC motor (PMDC) being the most common type of brushed electric motor in many commercial sectors.

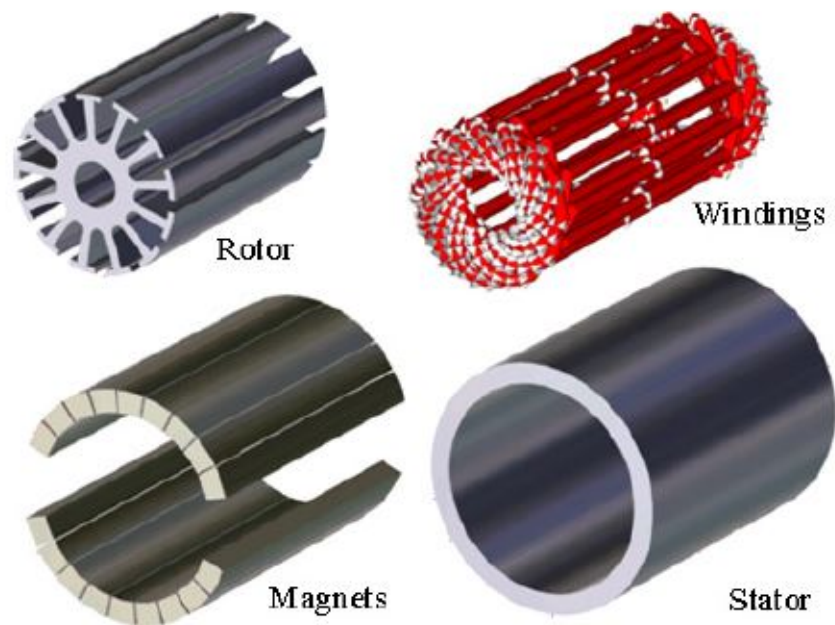


Figure 2.7: *Typical geometry of a PMDC motor [40]*

Brushless motors are characterized by the rotor being a permanent magnet and the stator having the coils. In this configuration, the magnetic field is controlled by adjusting the magnitude and direction of the current in the coils, which allows greater control and higher production of torque. AC motors can be synchronous or asynchronous (induction). The speed of the rotor equals the speed of the stator in the first subcategory, meaning that two

electric inputs are needed to make the machine start. AC induction motors don't need a double input and they can start by just supplying power to the stator.

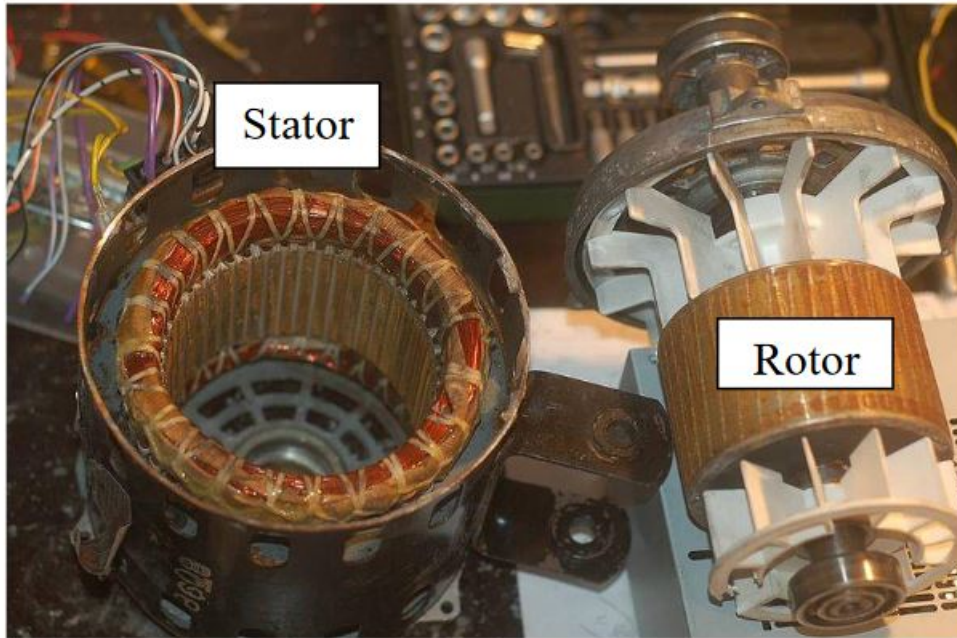


Figure 2.8: *Induction motor components [39]*

Chapter 3

Soft magnetic alloys

They constitute one of the main categories of magnetic materials. Magnetic materials have been known for several years, but a great impetus to their development was the discovery of the relationship between magnetic and electric fields in 1819 [57]. Today, magnets are extensively used in society, as crucial components in computers and other electronic devices, as well as parts of energy generation or transmission.

The two main classes of magnets are usually referred to as:

- hard magnets: they have high coercivity and a big area within the hysteresis curve (Figure 3.1); these magnets are used for those applications where the material is intended to keep the magnetization for long periods and resist the action of stray fields.
- soft magnets: they have small coercivity and a very narrow hysteresis area. These properties are fundamental for those applications where the field is reversed periodically because soft magnets are easy to magnetize and demagnetized.

The hysteresis curve shows the behavior of the material when the following experiment is performed: a magnetic field $[A/m]$ is gradually applied in the range between $-|H|$ and $|H|$ and the magnetic flux B $[T]$ is measured in the material. For both soft and hard magnets, there is a value of field that is strong enough for the magnetic flux not to change anymore. The corresponding maximum magnetic flux is called *saturation magnetization* (M_s). In the experiment, the applied magnetic field is reversed when M_s is reached in the material. When the applied magnetic field goes back to $H = 0 A/m$, there might be a non-zero magnetic flux in the material, which is called *remanence* B_r . The *coercivity* H_c is the applied field that is needed to get a zero magnetic flux. The coercive force is one of the main differences between soft and hard magnets, with a much greater magnetic flux required

in the latter case to get a zero flux.

Another difference is the overall area that is created during an hystereic cycle: this area represents the magnetic energy loss per unit volume per cycle. Soft magnets show a really small area, meaning that the amount of heat generted in the magnets during the cycle is low.

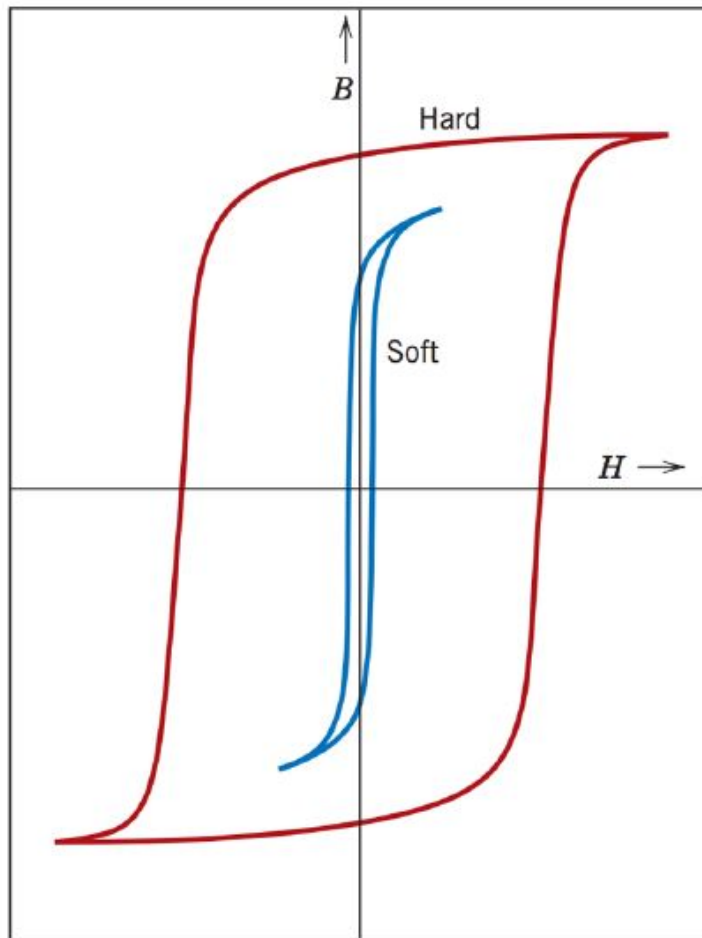


Figure 3.1: *Hysteretic curve: difference between hard and soft magnets [56]*

The difference between soft and hard magnets can be also expressed in terms of *permeability* μ , where μ is the ratio between B and applied H . Soft magnets exhibit very high permeability.

3.1 Applications of soft magnetic materials

Soft magnets are widely used in those sectors in which the field is reversed often. Thus, minimum energy loss per cycle is a priority requirement during material choice. This loss is also known as *core loss* and is explained in the following paragraph of this chapter.

Three main uses of soft magnets can be identified [58]:

- Heavy-duty Flux Multipliers: the cores of transformers, generators and motors fall in this category. These machines - working almost exclusively at 50/60 Hz - are usually large and heavy, then a material with high flux density and low cost per pound is required. Iron is often the choice for this application, with the industrial name of *electrical steel*.
- Light-duty Flux Multipliers: the cores of small machines for specific applications and electronic equipments fall in this second class. Since these machines have small/micro size, the requirement on cost per pound is not a priority, but it is secondary to some magnetic properties [58]. Frequencies may go up to the order of megahertz. Nickel-iron alloys and soft ferrites are common for these purposes.
- Microwave System Components. Soft ferrites are used for this class, too.

3.1.1 Eddy-currents

Minimum energy loss is a priority design objective when it comes to cores that are subject to alternating or rotating magnetic fields. This is the case of transformers, motors and generators.

The alternating/rotating flux generates a electromagnetic field not only in the secondary coil (transformers)/ rotor (motors/generators), but also in the core itself. If the core is a conductor, the induced electromagnetic field will create eddy currents. The consequences of eddy currents are the decrease of the flux and the production of heat, meaning that a power loss is happening. This power loss is proportional to i^2R [58], where i is the eddy current and R is the resistance of its path. Producing a laminated core - with thin sheets that are insulated from each other - is then beneficial to the reduction of core loss because of two reasons: not only the length of the path is reduced, but also the cross-sectional area is smaller than a solid piece. The decrease of the path length and of the cross-sectional area contribute to the reduction of R . Indeed, the laminated construction is a standard for this type of machines.

3.2 Common soft magnetic materials

Soft magnetic alloys can be classified into three categories:

- metallic alloys
- intermetallics
- ceramics

The selection of the optimal soft magnetic material for the specific application is based not only on the set of desired properties (permeability, electrical resistivity, coercivity, mechanical strength,...) but also on the cost [7]. For instance, alloys based on the intermetallic compound FeCo have high saturation magnetisation, but their spread is limited by the high cost of Co [7]. The following section aims to give a brief overview of the traditionally utilized soft magnetic alloys.

3.2.1 Electrical steel

This category is also referred to simply as *iron* and it includes low-carbon steel and silicon steel, both used for cores of electrical machines. The desired texture for these materials in terms of magnetic properties is achieved after recrystallization.

Low-carbon steel is characterized by a carbon content of about 0.03 %, thus it could be seen as pure iron with some undesired carbon impurities. It is widely used for the cores of small motors where energy loss is not a fundamental design objective, but power consumption (input) is [58]. Examples of these motors can be found in many household devices (vacuum, toys,...). Silicon steel falls in this category, too; Si-Fe alloys are often called *silicon iron*. The addition of silicon to iron is beneficial in terms of:

- electrical resistivity: the increase in resistivity results in a reduction of eddy currents and, thus, losses;
- magnetocrystalline anisotropy: the reduction of anisotropy makes the permeability increase.

However, the addition of silicon makes the alloy brittle, therefore it is difficult to roll into thin sheets by cold-rolling. This family of soft magnetic alloys is dominant in many types of low frequency large electric motor cores because of both their electromagnetic properties and their cost. 90% of low frequency applications is covered by Fe-Si alloys with low Si content ($\text{Si} < 3.25\% \text{ wt}$), that is produced by a conventional cold rolling technique

[7]. However, when increasing the Si content for high frequency electrical machines, expensive processes are needed to limit the increase in brittleness and the reduction in saturation magnetization if the alloy is produced conventionally. Many techniques [58] (electrolysis, direct vapor deposition, chemical vapor deposition) to reach 6% silicon content have been widely investigated for this magnetic alloy in order to increase the electrical resistivity and to decrease the magnetic anisotropy. AM could be an alternative, with no expensive treatment needed but an annealing of the printed part at a low temperature [7].

3.2.2 Fe-Ni Alloys

Nickel-iron alloys exhibit superior magnetic properties than Fe-Si alloys in terms of losses and permeability and they can be produced in very thin sheets. However, due to their high cost, their use is less widespread. The application sectors are those components where the cost is not a major consideration, while excellent magnetic properties are required.

The percentage of nickel can vary between 35% and 90%. 78% is a common nickel content for low-power transformers, while 50% nickel is used for high-power transformers. Other elements (e.g. molybdenum) can also increase the permeability [24] and the heat treatment is crucial for reaching the maximum permeability, too [7]. A common heat treatment consists in keeping an high temperature (1000°C) for a long period of time in hydrogen in order to remove impurities of C and S.

3.2.3 Fe-Co Alloys

Iron-cobalt alloys are characterized by the highest saturation magnetization and Curie temperature among soft magnetic materials [7], but their price reduces the application sectors to very specific fields. Alloys with cobalt content ranging from 30% to 50% exhibit saturation magnetization that is 10% higher than iron at room temperature. The mechanical, electrical and magnetic properties vary depending on the content of iron and cobalt and thus can be controlled by adjusting the percentages of Fe and Co and by adding alloying elements. As an example, the 50-50 alloy - commercialized under various names - has low anisotropy and high permeability, but it can develop order that makes it brittle. Ternary and quaternary alloys also exist: alloying elements such as V, Mo, Cu Mn, Cr are used to enhance some properties like corrosion resistance or ductility. As an example, small quantities of vanadium are often added to improve the ductility without decreasing the magnetic properties. High ductility is a key requirement when

a combination of magnetic properties and mechanical strength is required, because processing the material into thin sheets is typically needed to reduce electromagnetic losses [61].

Fe-Co are used in aircraft motors, generators, and transformers operating at 400 Hz, in beam-focusing lenses for electron microscopes [58] and in all those cases where high saturation magnetization or high Curie point (or both) is required.

3.2.4 Soft magnetic composites

Soft magnetic composites (SMCs) are magnetic particles of iron or high-magnetic materials that are insulating with a coated film after being consolidated under high pressure or other new techniques [25]. SMCs are used in conventional manufacturing methods to produce electrical cores as an alternative to laminated steel cores. They exhibit the unique property of three-dimensional ferromagnetic isotropic behavior [25]. The insulating coating results in low eddy current loss, at the cost of reduced magnetization and mechanical strength [7]. Producing SMC cores by AM processes may benefit from reduced weight and production costs and new flexible designs.

3.2.5 Soft ferrites

Soft ferrites have the general formula $MOFe_2O_3$ where M is a metal such as Mg, Mn or Ni. They are commercialized under various names and their manufacturers prefer to specify their magnetic properties instead of their composition. Soft ferrites are employed in high frequency applications, such as antennas, and they are characterized by low coercivity and extremely high electrical resistivity. They are not used in rotating electrical machines because of their low magnetization and brittleness.

Chapter 4

Additive Manufacturing processes

Additive Manufacturing (AM) is a process of "joining materials to make objects from 3D model data, usually layer upon layer" [26]. If the mass of the workpiece is considered, three main classes of manufacturing processes can be distinguished:

- subtractive processes where the mass is progressively reduced to achieve the desired geometry;
- formative processes where the workpiece shape is modified but the mass doesn't change;
- additive processes where the mass is increased. AM falls in this category.

The process chain of AM is explained in Figure 4.1, regardless of the specific technique.

The starting point of the process is the virtual three-dimensional CAD (computer-aided drafting) model, which can be obtained either by 3D CAD design or by reverse engineering (scanning technology). The 3D model is then converted into a universal standard language that is called Standard Triangulation Language (STL): the 3D solid model becomes a *shell* model by using triangles to approximate the external surface. Some errors can be generated during this conversion (gaps between cells, intersection of triangles,...), but this is still the most used and reliable standard at the moment.

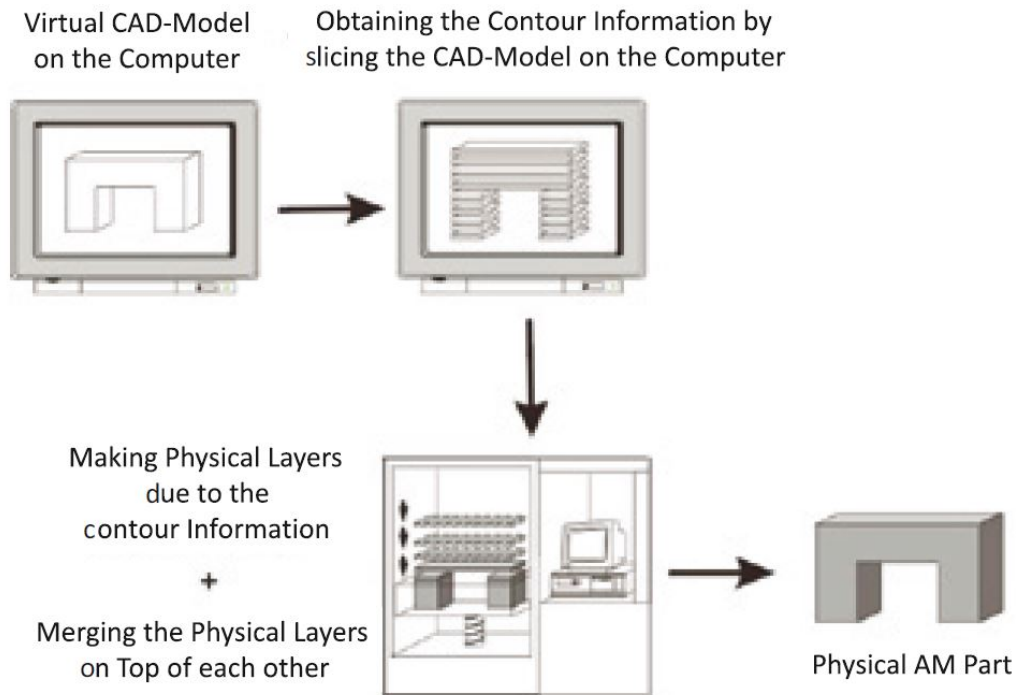


Figure 4.1: *Principle of additive manufacturing [53]*

The .STL file is preprocessed by using one of the available softwares (e.g. Insight) to perform the following steps:

- the part model is oriented into the building area by considering the geometry of the part and the use of support materials. In this step of the process, the shape is taken into account to minimize the effect of the layer-by-layer building manner on the roughness and to reduce the need for supports.
- Supports are added to both separate the part from the building base and to hold protruding geometries. Supports can either be of the same material of the part or of a different composition to facilitate their removal.
- The *slicing* is then performed on the software, meaning that the .STL model is virtually intersected by parallel planes with a constant or adaptive layer thickness. This second approximation of the geometry is the cause of the *stair stepping effect* that is better explained in the following sections of this chapter.

After the pre-processing steps are carried out on the software, the part is physically built in the AM machine. The way physical layers are obtained and merged on top of the previous one depends on the specific technology. In the end, some post-processing may be required to remove support material and improve the finishing.

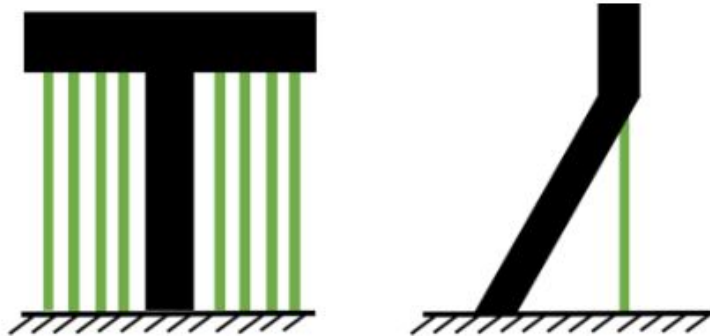


Figure 4.2: *Support material during AM: supports for printability (on the left) and supports for balance (on the right). Figure adapted from [54]*

4.1 AM potential and challenges

AM was previously known as "rapid prototyping", since it was a set of technologies used to 3D print models and prototypes, especially made of polymers. In the early stages of its introduction - a few decades ago -, AM was employed to speed up the last phases of the project and testing process, but it was not an alternative to the conventional fabrication techniques and its components were confined to non-functional parts. Despite the initial limits, AM showed immediately its potential in terms of reduced waste, fabrication costs and quasi-infinite freedom in design. Not only designers can create shapes that cannot be produced conventionally, but also the more complex the geometry is, the greater saving will result from using AM instead of traditional machining and tooling (Figure 4.3 by Hans Jorg-Dennig). The aforementioned advantages of AM constitute some of the reasons why researchers have been investing a lot in the development and the growth of AM, which is now a promising set of processes for end-use components made of either polymers and metals. The expansion of AM techniques to metals was one of the most crucial steps for its growth in terms of possible applications and thus markets.

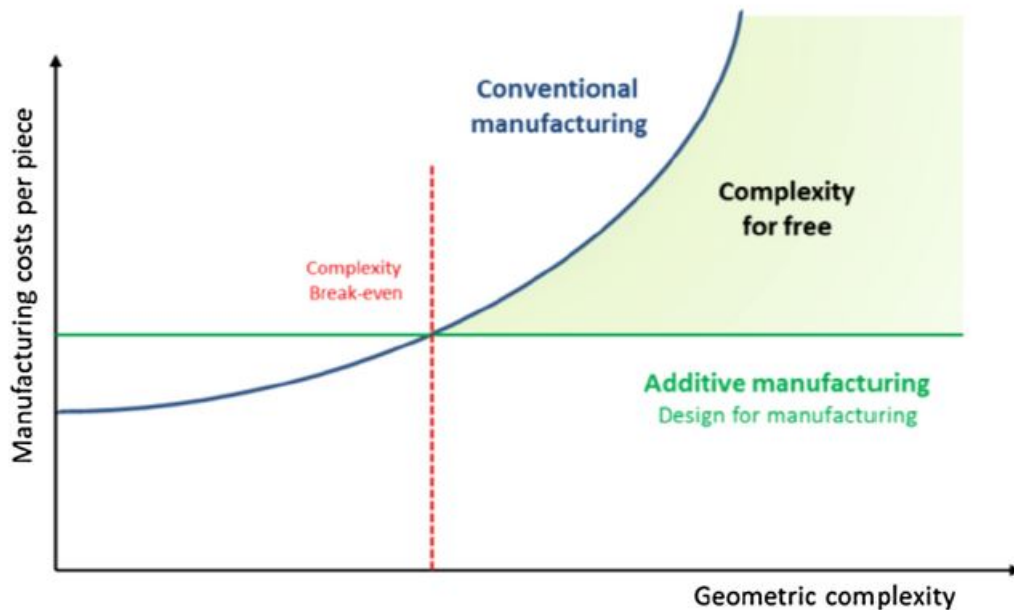


Figure 4.3: *Cost per piece vs geometric complexity in AM*

Although its potential, AM is not suitable for all applications due to its limited volume, low printing speed, availability and cost of materials, rough finishing. Even if one major advantage is that AM allows for the production of fully functional assemblies in just one step and by using only one machine, the assembly dimensions are constrained by the capability of the printing machine and the number of allowable materials on it, which is limited too. Another constraining factor consists in the lack of standard procedures and parameters in AM, meaning that engineers need to run experiments to come up with the optimal range for each parameters when producing a piece by AM. Not only the parameters, but also the orientation in the machine must be taken into account. More generally, the Design for Additive Manufacturing (DfAM) is really process-specific and it is not an adaptation of what has been already designed for conventional machines and tools. One main cause behind the lack of standardization is an insufficient understanding of what happens in the microstructure during an AM process, as a consequence of the sharp peaks in time-temperature plots [8]. The target properties will be then achieved through trial and error.

4.2 Classification of AM processes

AM techniques are regularly updated because researchers are constantly introducing new processes. A non-exhaustive scheme of the currently approved techniques is shown in Figure 4.4.

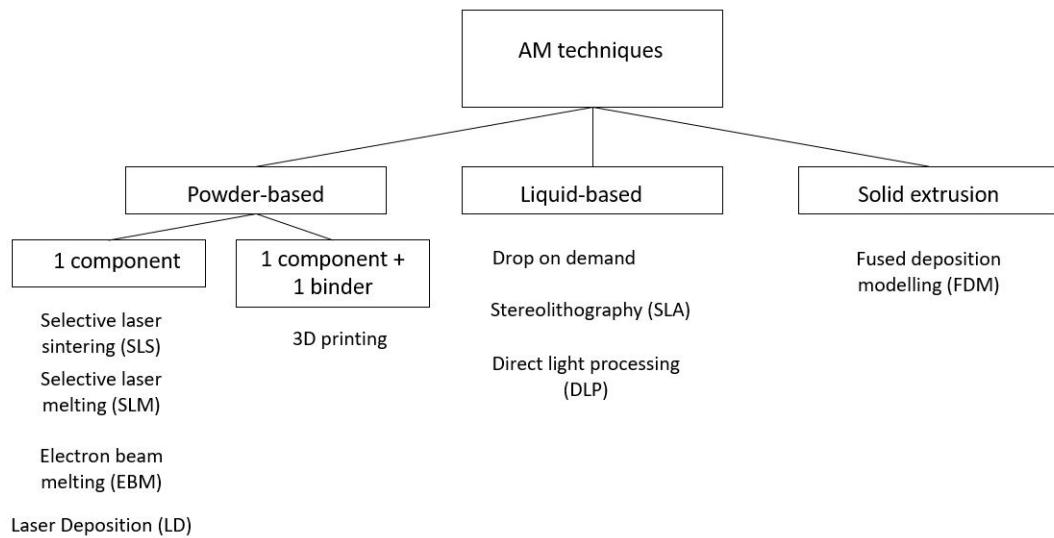


Figure 4.4: *Classification of additive manufacturing techniques*

As shown in the scheme, one major distinction depends on the feedstock material, which can be a powder, a liquid or a solid. Many different processes exist for each of them. For the purpose of this report, selective laser melting will be investigated more extensively in the next section, even if some research on electric machines can be found in the literature by other techniques, namely FDM, binder jet technology (BJT) and laminated object manufacturing (LOM). The LOM method can be considered as a hybrid technique since it involves both layer addition and extensive cutting and machining. SLM is a powder bed fusion (PBF) method using laser as heat source.

Figure 4.5 illustrates the difference in the working principle between PBF techniques and Direct Energy Deposition (DED) processes. In the latter case, the feedstock material is added directly to the melt pool and a heat source is applied to a narrow region to simultaneously melt the substrate and the feedstock material. An example of DED is Laser-Based Metal Deposition (LBMD).

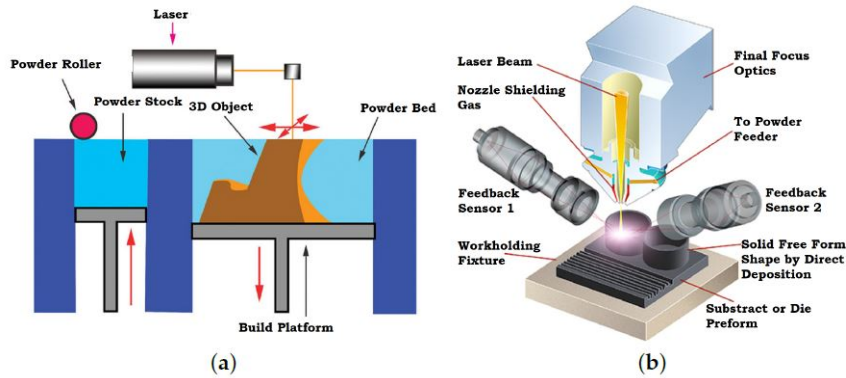


Figure 4.5: Working principles of PBF and DED processes [49]

4.3 AM defects

Using an AM technique to produce a component may benefit from numerous advantages during all the stages of the lifecycle of a product (design, production, usage), but some drawbacks of AM processes must be considered and/or mitigated to make a part acceptable. Figure 4.6 from reference [28] shows a summarizing comparison between AM and conventional techniques.

Defect	Process PBF/DED	Description	Inspection Methods
Vaporization of Alloy Elements	Both	Loss of alloy elements due to vaporization compromises mechanical strength	X-Ray EDS (NDI) EPMA (NDI) ICP mass spectrometry (DI)
Porosity and voids	Both	Quality Powder: Hollow powder (gas entrapment) Process instabilities (keyhole voids, lack of penetration, ...)	X-Ray CT (NDI) SEM (NDI)
Surface Roughness	Both	"Stair step effect", humping effect and powder poor melting	Profilometer (NDI) SEM (NDI)
Cracking	Both	Uneven contraction of deposited material builds up stress until strength limit originating fracture	Vickers micro-indentation (Indirect measure and DI) Hole drilling combined laser holography and/or strain gauges (DI) X-Ray and Neutron diffraction (NDI)
Delamination	PBF		ECT (NDI)
Distortion	Both	Residual stress leads to strains → Out of tolerance	Conventional Metrology (NDI)
Trapped Powder	PBF	Hollow Structures needs powder extraction points	CT (NDI) RT (NDI)

NDI, Non-Destructive Inspection; DI, Destructive Inspection; EDS, Energy Dispersive Spectroscopy; EPMA, Electron Probe MicroAnalysis; ICP, Inductively Coupled; CT, Computed Tomography; SEM, Scanning Electron Microscopy; ECT, Edge Current Testing; RT, Resonance Testing.

Table 4.1: AM part common defects and inspection methods

Some common defects of AM process are listed in Table 4.1 above from [49], together with their inspection methods.

	Additive Manufacturing Technology	Traditional Manufacturing [19]
Cost	Products can be manufactured at comparatively low costs; this is however limited to small and medium production batches.	These methods are expensive for small production batches. As costs are involved in casting molds, dyes, tooling, finishing and other different processes that goes into manufacturing the products.
Time	Products can be manufactured in a very short time. As AM makes products directly from the CAD model, it helps save time in delivering end products by cutting down on the production development step, supply chain and dependence on inventory.	Manufacturing times are very long, as it depends on the availability of the molds, dyes, inventory etc.
Resource Consumption	Only optimal quantity required to manufacture the product.	Extremely high.
Product Complexity	Used to manufacture complex geometries and products. The products are only limited by the design engineer's imagination.	Complex geometries cannot be manufactured. Many different parts have to be manufactured separately and assembled post manufacturing.
Post Fabrication Processing	Little to no post-fabrication processing is required, depending on the technique and material used.	A majority of the time, some kind of post-processing is required.
Material Quality and Application	The material quality depends on the technology used. Initially 3D manufactured parts were not used in load bearing application, but advancements in the technology is rapidly improving the material quality which has led to them being used in some load bearing applications.	Due to their excellent quality, the products have always been used for load carrying applications.
Material Wastage	There is little to no wastage of the raw material, as they can be reused.	Involves a lot of material wastage due to post-fabrication finishing processes.
Prototyping	Extremely useful for prototyping and evaluating product concepts. Allows for design changes and iteration.	Very expensive and time consuming. Not preferred for product prototypes and concepts.
Space Application	3D printing could essentially pave the way for setting up structures off-world, especially on the Moon and Mars.	It will be exorbitant to build structures off-world using these techniques.

Figure 4.6: *Comparison between additive techniques and traditional techniques*

A defect that can occur both in DED and PBF processes is the vaporization of alloying elements as a consequence of the high temperature reached in the melting pool and of the difference of volatility among elements. The

loss of alloying elements influences the chemical composition and negatively impacts on the mechanical properties of the part. The prediction of this defect is not straightforward, because an increase in temperature would facilitate the vaporization but also make the melt pool bigger and more stable. Another issue concerning alloying elements is the micro-structural lack of homogeneity, because of elements' segregation into the grain boundaries. Surface roughness is another characteristic of additively manufactured parts that may make the component unacceptable or may require post-processing. One main cause for this defect is the *stair stepping effect* which is inherent in any AM process because of the layer-by-layer nature of these techniques. A conceptual representation of it is shown in Figure 4.7 [50]: the CAD model of the part is approximated by using a software. A limited number of layers is used in the approximation of the geometry with the resulting slicing effect. The surface roughness will be greater on curved surfaces. A mitigation strategy consists in reducing the layer thickness, with a consequent increase of building time.

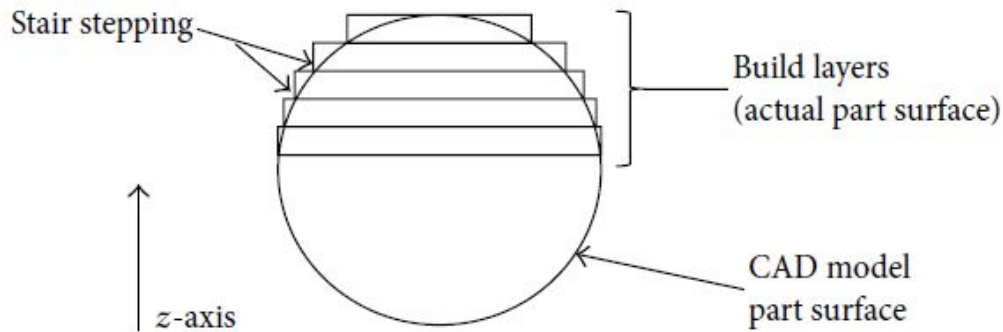


Figure 4.7: *Conceptual representation of the stair stepping effect*

The humping phenomenon and the poor powder melting, instead, are parameter-related causes for surface roughness. Lack of powder fusion is also the reason for another undesired effect in AM components that is porosity.

AM workpieces can have different pores and voids, which are usually the result of a not well-controlled process. Porosity is usually undesirable, since it can bring to premature failure of mechanical components. However, sometimes it is the consequence of a careful selection of process parameters [51] to intentionally produce surface-breaking pores that allow for a better biological integration of biomedical implants.

Cracking and delamination (Figure 4.8) are also very common during AM

processes. The rapid heating and cooling cycles and the uneven contraction of layers during solidification cause thermal strains that can result in cracking and delamination (this latter phenomenon can happen only in case of PBF processes). Those defects are facilitated by the presence of elements' segregation along grain boundaries. Even if stress doesn't always reach the threshold for the workpiece to crack or delaminate, the resulting distortion is one of the main reasons for non competitive final parts [49].

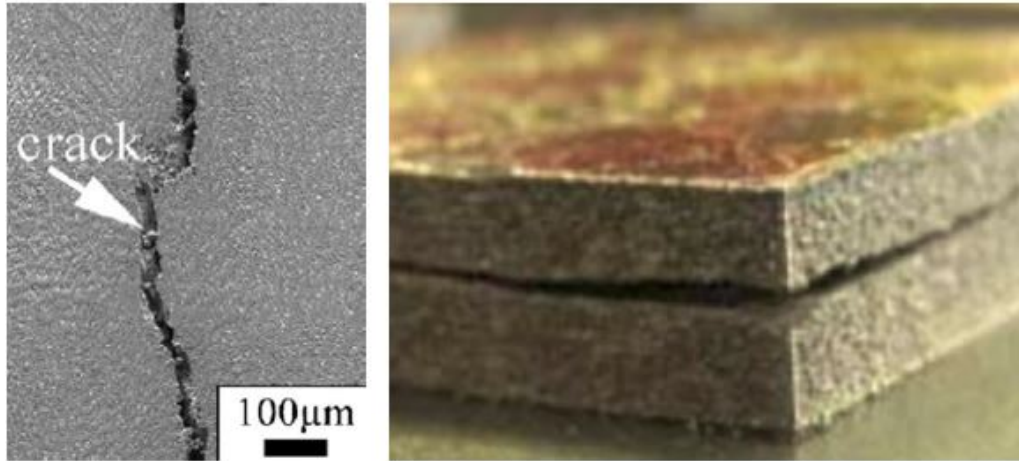


Figure 4.8: *Cracks (on the left) and delamination (on the right) of AM parts. (Illustration adapted from [49])*

Finally, trapped powder is a typical negative effect of hollow shapes that are produced by PBF techniques. In these cases, extraction points must be included in the design of the part.

4.4 SLM

Selective laser melting (SLM), also known as laser powder bed fusion (LPBF), is a powder-based technique to additively manufacture metal components. The heat source that allows the metallic powders to fully melt is an high intensity laser. The concept of the process is represented in Figure 4.9 from [32]:

- a layer of powder is laid on the bed and then paved;
- the heat source is used to selectively melt some areas in the x-y plane according to the CAD file;

- another layer is deposited after the building plate is lowered in the z-direction through a piston.

The process continues automatically in a layer-by-layer fashion until the component is fully built. Sintering processes generally don't require any bases or supports because the loose powder acts as a support. However, this is true in the case of plastic processes, while metal parts are an exception [53] and supports are needed to prevent warping.

In the end, the part can be removed from the substrate plate either manually or by electrical discharge machining (EDM) and the loose powder is removed, too. Nitrogen gas or argon gas are usually used inside the chamber to give an inert atmosphere and prevent oxidation. The chamber is also equipped to handle inflammable materials, such as titanium or magnesium while built-in heating devices help to reduce distortion of the part [53].

A major advantage of SLM consists in fully melting the powders and thus giving a 99.9% dense, near net-shape component [32], with better resolution than other AM methods [13].

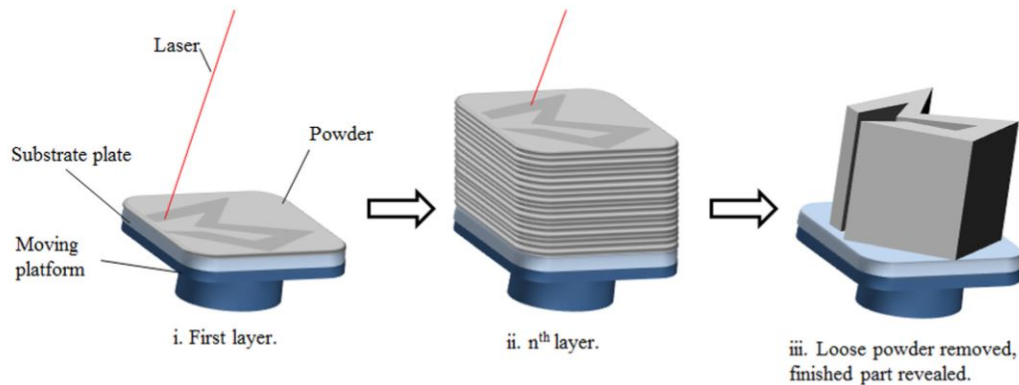


Figure 4.9: *Concept of SLM*

Literature demonstrates that a proper choice of the process parameters can result in comparable or superior mechanical properties to those of bulk materials, also in case of powder mixture [17]. However, despite its great advantages, there is still a lack of standardization that is holding back SLM from widespreading at full potential. Before reaching the target properties, the techniques of design of experiments (DoE) are often used to establish the optimal ranges for each parameter since the rapid heating, melting and cooling that happen during an SLM process make it difficult to predict and sometimes even understand the relationship between parameters and result-

ing properties. The next section of this chapter aims to give an overview of the most important SLM process parameters.

4.4.1 SLM process parameters

Laser power, scanning speed, hatch spacing and layer thickness are the parameters that are adjusted during the SLM process to achieve the target (Figure 4.10).

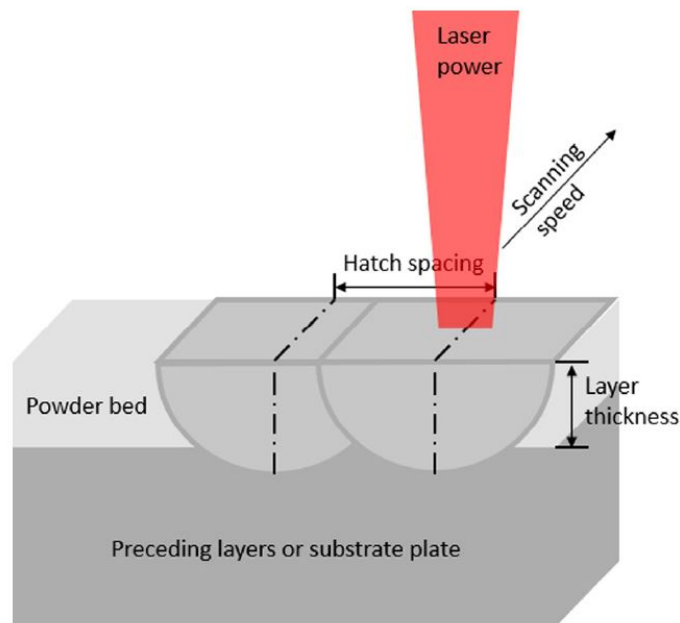


Figure 4.10: *Illustration of SLM process parameters [32]*

The building orientation is also considered in the literature because of its strong influence on the mechanical behavior (strength, fatigue resistance, elongation) as shown in [17] for 316L austenitic stainless steel. The building orientation has also a significant impact on the morphology of the molten pool boundaries (MPBs). In the study [9], MPBs are investigated as a result of the orientation to explain the characteristic higher strength and anisotropy and the lower ductility of SLM components if compared to conventionally manufactured parts. A good choice of the parameters can limit the typical defects of SLM parts, namely internal voids, partially melted powder and residual stress. Heat treatments help in reducing residual stress [18] and in reaching the target magnetic properties [7]. Disparate studies in the literature demonstrate that a low energy - resulting from low laser

power, large layer thickness and high scanning speed - can cause *balling*, a particular phenomenon in SLM where spheroidal beads obstruct the formation of continuous melt lines [32]. On the contrary, high laser power and low scanning speed may cause material evaporation and thus a change in the chemical composition accompanied by the keyhole effect. An illustration of the process of keyhole formation is shown in Figure 4.11. An high laser power results in a long keyhole and in laser scattering inside it. The pore formation results from the collapsed keyhole, after metal evaporation [19].

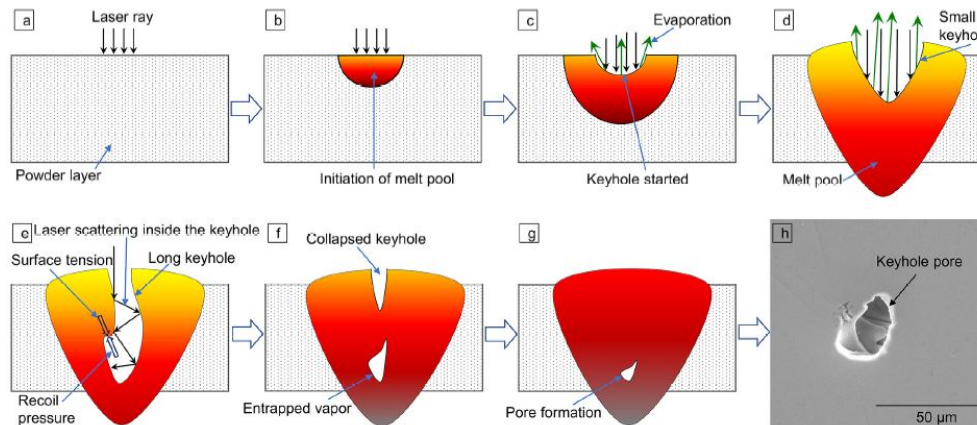


Figure 4.11: *Illustration of keyhole formation [19]*

Finally, the hatch spacing has been highly investigated in the literature. It has a great influence on the heat-transfer behavior, relative density and surface quality [33]. An increase in the hatch spacing results in a reduced peak of temperature and heat accumulation with effects on the microstructure. The microstructure can also be predicted by simulation models that can support the appropriate choice of this parameter in order to get a good surface quality and high relative density (99.9%) [33].

Clearly, strong process-structure-properties relationships characterize SLM; however, a more solid understanding of the phenomena involved in the process is fundamental to predict the properties based on the parameters. Sometimes, process-structure-properties relationships available for welding are used as a reference, since some AM methods have the same heat sources as welding processes [8], but the error and trial is still the most reliable way of finding the optimal ranges for the process parameters.

4.4.2 Residual stress in SLM produced parts

One of the main SLM process consequences is the high residual stresses remaining in the part after its fabrication. Indeed, SLM is similar to a laser welding process and, particularly, to a laser cladding with feeding material provided in powder form [56]. One main difference is the size of the melting pool, that is way smaller in the case of SLM, thus giving finer structures. Consequently, with an optimal choice of the process parameters, pores can be avoided. However, the local solidification of molten regions causes significant stresses in the printed component. The effects of the remaining stresses - namely deformation, cracks, loss of static and dynamic strength - can be unacceptable for the intended scope of the part.

High residual stresses occur in SLM parts because of high temperature gradients. During the process, the material undergoes repeated heating and cooling, but the volume is not free to expand and contract due to the metallurgical connection with adjacent or underlying material.

Two models can be found in the literature describing the mechanism of formation of residual stresses during SLM: both theories are based on the expansion behavior of the material during thermal cycles [56]. The temperature gradient mechanism (TGM) explains how the stress is induced in a single melt track because of the connection to adjacent colder tracks. Instead, the cool-down mechanism describes the expansion behavior resulting from the temperature difference between one melted powder layer and the underlying layer. The TGM concept is illustrated in Figure 4.12 below.

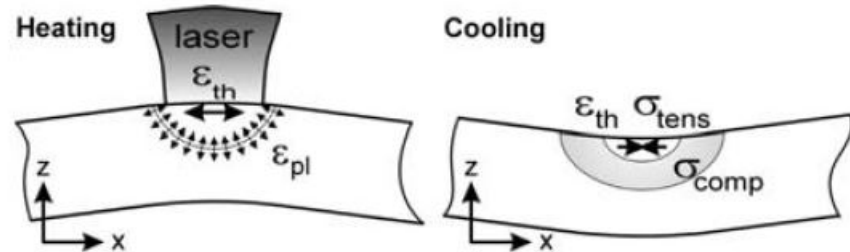


Figure 4.12: *Explanation of the temperature gradient mechanism [57]*

As shown in the illustration, the laser beam provides heat to the material causing the thermal expansion of the track. The adjacent material is colder than the track being heated and melted by the laser, thus inducing elastic compressive stresses in the heat affected zone [56]. Plastic deformation or upsetting of the material in the direction of the laser occur when the yield strength is overpassed, with a consequent reduction of stresses.

During the cooling phase, the track cools down and contracts. However, due to the surrounding material, tensile stresses are generated in the plastically deformed area with bending occurring in the opposite direction to the energy source.

Similarly, the cool-down mechanism describes the stresses generated because of the temperature gradients between two subsequent layers. As illustrated in Figure 4.13, the top layer has an higher temperature than its previous one. During cooling of the top layer, it tends to contract more than the underlying layer, thus causing tensile stress in the upper bed and a compressive state in the bed underneath it because of their connection. The subjacent layers have usually a moment of resistance high enough to prevent plastic deformation; as a result, remaining tensile stresses are very high and when the tensile strength of the material is reached, cracks and voids may form in the part.

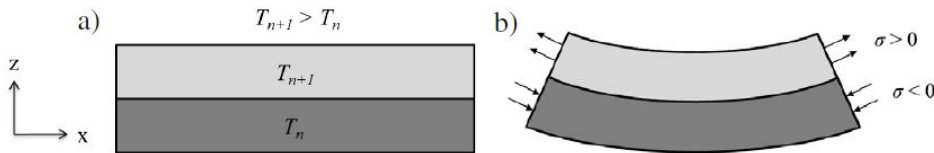


Figure 4.13: *Illustration of the cool-down mechanism [56]*

Many methods exist to investigate residual stresses, with both destructive and non-destructive (NDTs) tests. X-ray diffraction (XRD) is one of the most common among the NDTs and allows to investigate residual stress on the outer faces, but also at different depths in the part. Before explaining its working principle, the classification of residual stresses is required. Indeed, residual stresses can be divided according to the length scale where they occur [58]:

- type I: macroscopic stresses;
- type II: microscopic stresses occurring over the grain scale because of the presence of different phases in the part;
- type III: microscopic stresses occurring inside a grain because of defects.

The type I can be considered as an average of the stresses in a volume that is large enough to contain grains of all the phases formed in the material. Instead, while type II and III can be seen as a deviation from the

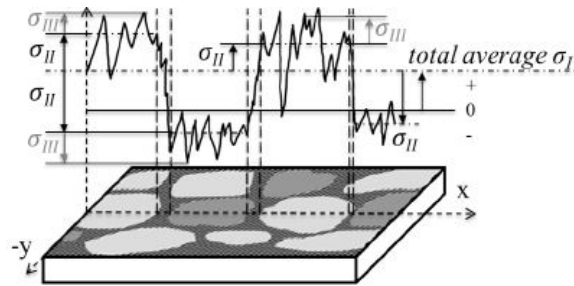


Figure 4.14: *Types of residual stresses [56]*

macroscopic (average) type I. The illustration of the aforementioned types is given in Figure 4.14.

The XRD examination is applied to investigate macroscopic residual stresses, because they cause a shift of the diffraction angle of the diffraction reflex [56].

Chapter 5

Traction electric motors produced by AM

The purpose of this last Chapter is to give an overview - to the best of the author's knowledge - of the state of art of electrical machines additively produced for automotive applications. A review of the literature shows that there is a great interest in the possibility of fabricating electric motors by AM, since the manufacturing method is more or less the same as what was used in the 1970s. The resulting design of the electric motor is then constrained by the conventional process. So far, all the research in this area has focused in demonstrating the suitability of AM for this application and, more specifically, in showing that the mechanical and electromagnetic properties are comparable to those of a traditional motor when the electric machine is produced by AM and made of one of the materials available for an AM process. Therefore, most of the studies are a characterization of one or more materials that may be suitable for this application: most of those works consider either many electromechanical properties at the same time or just one of them, and adjust the parameters of the process to reach the desired features [4][7][8][9][13][14][15][17][18][19][27].

Few studies have actually AM-produced a traction electric motor - or at least part of it - but they still investigate similar designs to the conventional one, with the objective of testing the properties on the component instead of just samples [1][35]. As yet, no study has shown the printability of a fully functional electric motor in only one step even if a great effort has been put in the fabrication of AM electromechanic devices, where electronic components are embedded in the part during production. An interesting study [34] demonstrate how it would be possible to fabricate an electric motor in a single sequence build, but with some pauses to allow for the

integration of bearings, windings, magnets, speed controller. The pauses in the process are shown in Figure 5.1.

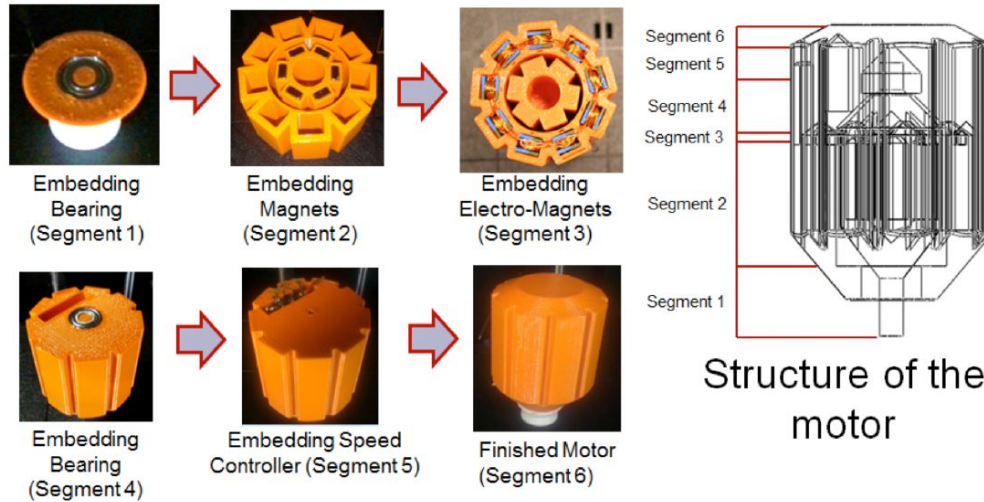


Figure 5.1: Illustration of the pauses during one-sequence build of an electric motor from [34]

This study opens up to new design possibilities, even if the testing of the motor (Figure 5.2) shows that its properties are still poor.

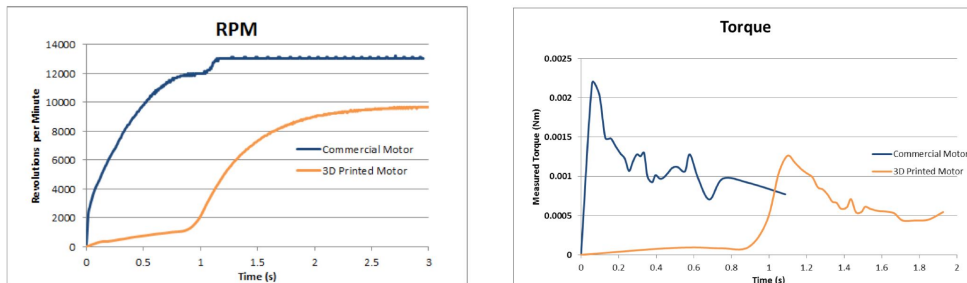


Figure 5.2: Results of a 3D-printed 3-phase brushless DC motor [34]

Another recent research [35] has focused on the cores and, more specifically, on the rotor (Figure 5.3): Fe-Co powder was used to SLM produce a rotor, with promising results in terms of mass density and saturation magnetic flux. However, the resistivity was not high enough to mitigate the losses.



Figure 5.3: *Illustration of an SLM-produced rotor [35]*

A similar study [1] was conducted on the stator (Figure 5.4), as explained in the Introduction, with the overall performance of the motor not being fully comparable to that of a conventionally produced machine.

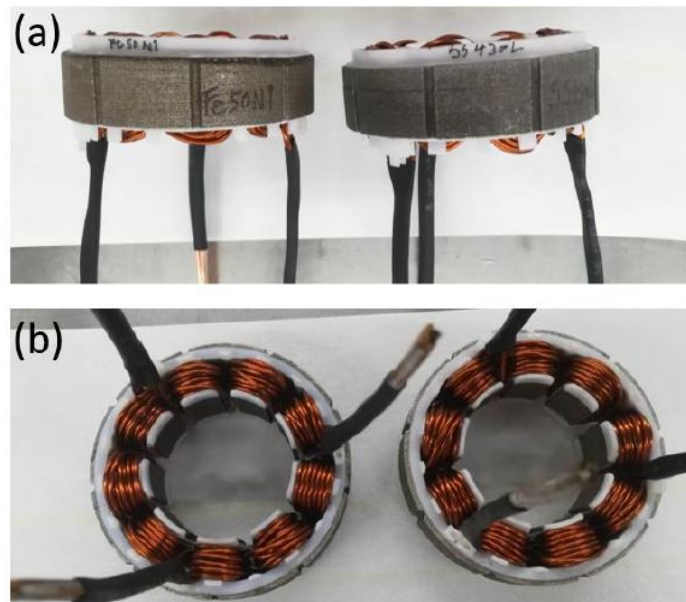


Figure 5.4: *Illustration of SLM-produced stators [1] made of two different materials*

Chapter 6

Finite Element Analysis (FEA) of rotor

One method to continue improving in the sector of additive manufacturing applied to electric cores consists in using numerical simulation instead of physical printing, at least in the early stages of a research. In this work the prediction of residual stress on a rotor produced by SLM is conducted by using ANSYS 2020 R2 software with its additive tools. Some advantages of simulating are listed below:

- thermal distortion and residual stresses can be investigated;
- the engineer can come up with the best orientation of the part on the build base and the optimal supports to use;
- the designer can understand if the part is physically buildable and how the design can be modified to compensate for distortion.

The ANSYS Workbench simulation consists of a thermal-mechanical FE analysis with the thermal transient analysis being run first and the structural analysis subsequently, with the full thermal history data. The main stages of the process can be simulated in the software, namely preheat, build, cooldown, removal of the plate and supports. The procedure is explained in details in this chapter.

The FE analysis of an AM process has also the great advantage of investigating the influence of process parameters on the results (residual stress and deflection) without the need of wasting material in a physical printing of samples. This study extensively benefits from this advantage, as shown in the next chapter. However, one drawback of the simulation is that the software does not take into account the scanning strategy, which may have a significant influence on the results. The investigation of its influence needs

to be held necessarily by physical experiments, while some results of the numerical simulation must be critically discussed to consider how the scanning strategy impacts.

6.1 Geometry

The geometry for the simulation was created in Solidworks and it consists of an electric rotor with 12 slots, characterized by an height of 16 mm and an outer diameter of approximately 75 mm. The build plate base was created as a simple parallelepiped of 280 mm x 280 mm x 10 mm, which is a common size for the plate of SLM machines. The 3D CAD model of the electric rotor was downloaded from the free library of GrabCAD [63] and adapted for this study. The rotor geometry was modified to eliminate details in the shape that would have created stress concentration. For the purpose of this work, those details were not essential and would increase unnecessarily the computational time. The simplified geometry is shown in Figure 6.1. It can be noticed that the build part is oriented to align the build direction with the z-direction of the model. The local coordinate system is oriented so that both the supports and the build part have positive z-values, while the base plate is in the negative z-direction.

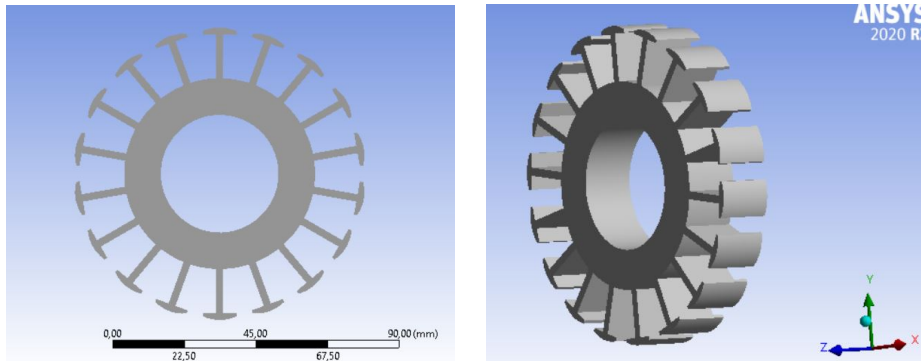


Figure 6.1: *Geometry (on the left) and orientation (on the right) of the rotor*

A gap of 2 mm was left between the build part and the base to allow for support generation in between. This step is performed directly in ANSYS Mechanical and not in the model generation. There is no need to represent the powder in this stage either, unless the analyst is interested in studying what happens in the powder, too. The powder is introduced implicitly later in the simulation by adding an heat convection coefficient for it.

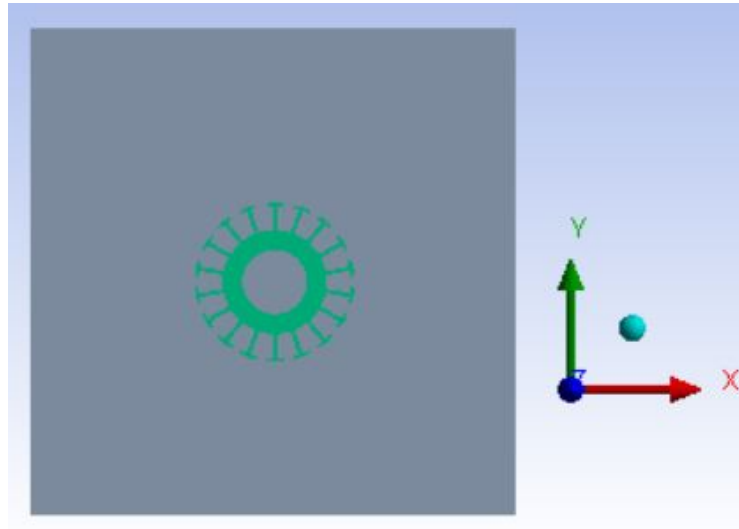


Figure 6.2: *Geometry and orientation of build plate base and rotor*

6.2 Material properties and build settings

Once the geometry is created, ANSYS Workbench is used to enter the material for both the build part and the base in Engineering Data. The material can be either one available in the library or a new material. In the latter case, some properties need to be specified as a function of temperature, in a range that goes from room temperature to near melting temperature. The material for the plate base was chosen to be maraging steel, which is common in many SLM machines.

Alloy	C	Ni	Co	Mo	Ti	Al	Mn	Si
18NiCo(200)	≤ 0.03	18	8.5	3.3	0.2	0.10	≤ 0.10	≤ 0.10
18NiCo(250)	≤ 0.03	18	8	4.8	0.4	0.10	≤ 0.10	≤ 0.10
18NiCo(300)	≤ 0.03	18.5	9.0	4.8	0.7	0.10	≤ 0.10	≤ 0.10
18NiCo(350)	≤ 0.03	18	12	4.2	1.5	0.10	≤ 0.10	≤ 0.10
13NiCo(400)	≤ 0.03	13	15	10	0.2	–	≤ 0.10	≤ 0.10
18NiCo(500)	≤ 0.03	8	18	14	0.2	–	≤ 0.10	≤ 0.10

Table 6.1: *Typical maraging steel compositions*

Its properties were taken from open literature and used to create a new material in the ANSYS library. Maraging steels are a class of low-carbon

steels that derive their ultra-high-strength from the precipitation of inter-metallic compound. They have very stable properties and retain their properties at mildly high operating temperatures. Typical nominal composition for maraging steels are listed in Table 6.1 above from [1]. During the simulation, it was assumed that there was no thermal strain effect in the build plate base, since there is no interest in its thermal-to-structural analysis. Then, the properties of the material for the base were not needed as a function of temperature, but they could be indicated as a single value, as shown in Figure 6.3.

1	Property	Value	Unit
2	Material Field Variables	Table	
3	Density	8100	kg m ⁻³
4	Isotropic Secant Coefficient of Thermal Expansion		
5	Coefficient of Thermal Expansion	1,01E-05	C ⁻¹
6	Isotropic Elasticity		
12	Strain-Life Parameters		
20	S-N Curve	Tabular	
24	Tensile Yield Strength	758	MPa
25	Compressive Yield Strength	1034	MPa
26	Tensile Ultimate Strength	4,6E+08	Pa
27	Compressive Ultimate Strength	0	Pa
28	Isotropic Thermal Conductivity	15	W m ⁻¹ C ⁻¹
29	Specific Heat, C _p	450	J kg ⁻¹ C ⁻¹

Figure 6.3: *Maraging steel properties for the build plate*

The material assigned to the rotor is 316 stainless steel, which is one of the available materials in the AM library of ANSYS. A typical nominal composition of 316 stainless steel is detailed in Table 6.2 below.

Grade		C	Mn	Si	P	S	Cr	Mo	Ni	N
316	Min	-	-	-	0	-	16.0	2.00	10.0	-
	Max	0.08	2.0	0.75	0.045	0.03	18.0	3.00	14.0	0.10
316L	Min	-	-	-	-	-	16.0	2.00	10.0	-
	Max	0.03	2.0	0.75	0.045	0.03	18.0	3.00	14.0	0.10
316H	Min	0.04	0.04	0	-	-	16.0	2.00	10.0	-
	max	0.10	0.10	0.75	0.045	0.03	18.0	3.00	14.0	-

Table 6.2: *Typical 316 stainless steel compositions*

The material choice was motivated by the presence of many studies about 316 stainless steel to compare the results and use the process parameters found in the literature. Since the objective of the study is the

investigation of the coupled thermal and structural analysis of the part, the properties of this material are required as a function of temperature, as described above. This is exactly the way thermophysical properties (density, thermal conductivity, specific heat capacity, elasticity, tangent modulus and Poisson's coefficient) are indicated in ANSYS Engineering data when a material is listed as AM material. As an example, the density curve taken from ANSYS AM library is shown in Figure 6.4 for 316 stainless steel.

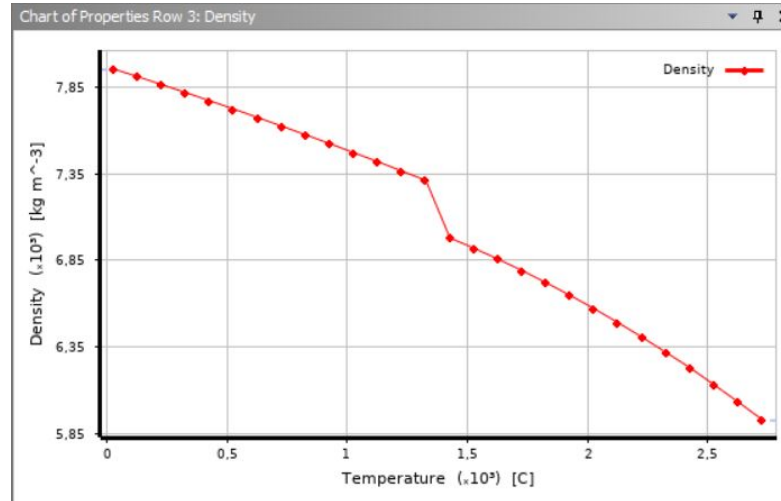


Figure 6.4: *Density curve for 316 stainless steel from ANSYS Engineering Data*

Once the materials and geometry are imported, the model can be launched from the transient thermal block of ANSYS Workbench and this opens ANSYS Mechanical.

The following steps must be performed before running a thermal-to-structural simulation:

- the material is assigned to all components of the 3D model;
- an AM box is introduced in the model and the build part and base are specified in the AM box;
- the reference temperature of the printed part is set to the melting temperature of its material;
- the build settings are specified (deposition thickness, hatch spacing, laser scan speed,...). During this step, a convection coefficient is introduced not only for gas but also for powder to implicitly represent the powder without modelling it in the 3D geometry;

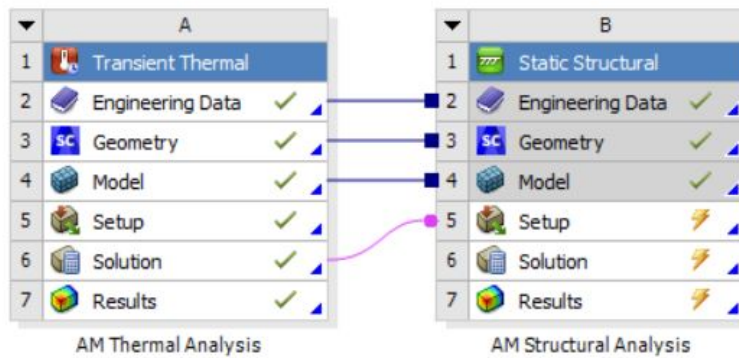


Figure 6.5: *Coupled transient thermal and structural analysis in ANSYS Workbench*

- the meshing is performed by using a cartesian mesh method for the build part: this choice aims to approximate the geometry in a layer-by-layer manner as it happens during 3D printing;

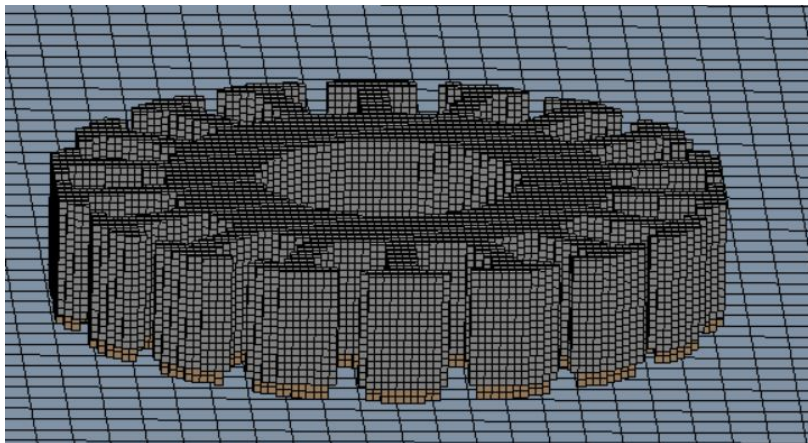


Figure 6.6: *Cartesian mesh of the rotor*

- the support toolbar is used to automatically generate supports between the base and the part as well as wherever the angle is greater than 45;
- the last steps consists in creating the base-to-build contact, which is another tool of the AM process box available in ANSYS.

Once all these steps are performed, the simulation is ready to be run as explained in the next paragraphs of this chapter.

6.2.1 Process parameters

The process parameters were set to the following values, as also shown in Figure 6.7:

- deposition thickness: 0.03 mm;
- hatch spacing: 0.07 mm;
- scan speed: 800 mm/s;
- preheat temperature 40°C;
- gas convection coefficient: 0.00006 W/ °C mm²;
- powder convection coefficient: 0.00003 W/ °C mm² ;

Details of "Build Settings"	
Machine Settings	
Additive Process	Powder Bed Fusion
Inherent Strain	No
<input type="checkbox"/> Strain Scaling Factor	1,
<input type="checkbox"/> Deposition Thickness	3,e-002 mm
<input type="checkbox"/> Hatch Spacing	7,e-002 mm
<input type="checkbox"/> Scan Speed	800, mm/s
Dwell Time	10, s
Dwell Time Multiple	1,
Number of Heat Sources	1
Build Conditions	
<input type="checkbox"/> Preheat Temperature	40, °C
Gas/Powder Temperature	Use Preheat Temperature
Gas Convection Coeff	6,e-005 W/mm ² .°C
Powder Convection Coeff	3,e-005 W/mm ² .°C
Powder Property Factor	1,e-002
Cooldown Conditions	
Room Temperature	22, °C
Gas/Powder Temperature	Use Room Temperature
Gas Convection Coeff	6,e-005 W/mm ² .°C
Powder Convection Coeff	3,e-005 W/mm ² .°C
Discretization Settings	
Layer Height	Program Controlled

Figure 6.7: *Process parameters*

Those values were taken from the literature with the objective of obtaining a full-dense part, which is usually the primary target when SLM-printing a component. The set of parameters aforementioned was used in the first part of the study. Subsequently, the parameters were changed to run a sensitivity analysis and evaluate the effect of different energy density values.

6.3 Transient thermal simulation

The first part of an AM FE simulation consists of a transient thermal analysis that requires as unique (thermal) load the temperature at the bottom of the build plate base. The temperature at this face is set to be equal to room temperature. During the thermal analysis, a temperature track plot can be activated to follow the simulation.

6.4 Static structural analysis

The second part of an AM FE simulation is the static structural analysis having as input both the thermal history (from the transient thermal analysis) and a constraint at the bottom of the building base (fixed support) as shown in Figure 6.8.

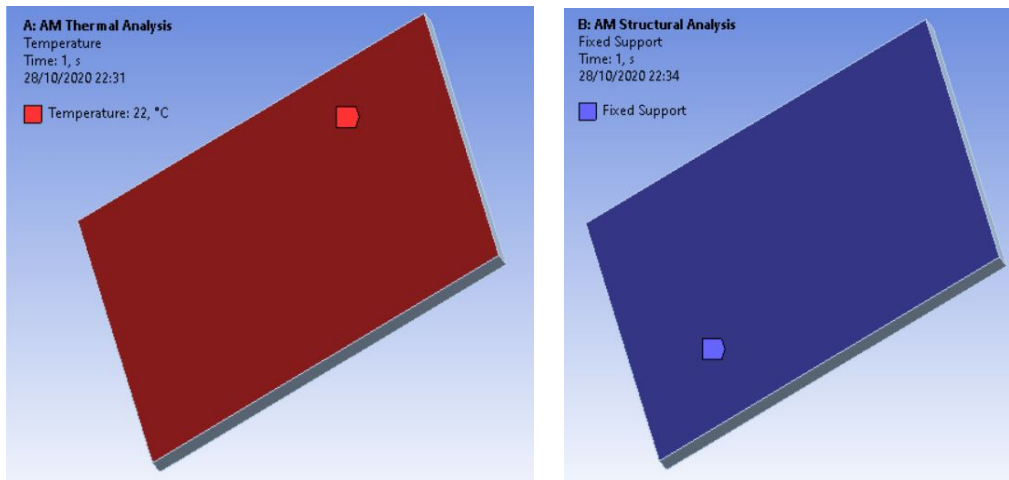


Figure 6.8: *Boundary condition for transient thermal analysis (on the left) and static structural analysis (on the right)*

One last phase before launching the analysis is the specification of the steps that the analyst is interested in studying. For the purpose of this study, the following steps were considered (Figure 6.9):

- build step;
- cooldown step;
- removal of the base;
- removal of the supports.

The final steps - removal of both base and supports - were included because they can affect significantly the residual stress and final distortion in the part. The way they affect the results is also dependent on the way the part is constrained during the removal step. It was assumed that the part was free to deform during that final phase.

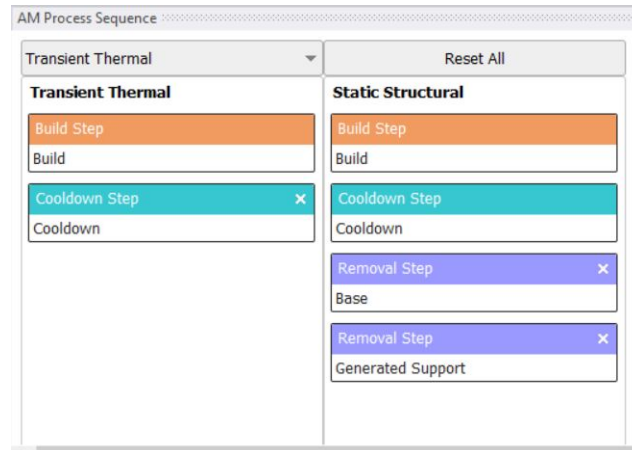


Figure 6.9: Step of thermal and structural analysis

Chapter 7

Results of FEA

The purpose of the current chapter is to illustrate the outcomes of the FE analysis applied to the rotor, as described in *Chapter 6*, and to compare the simulation results to the theory of residual stress in SLM. The equivalent stress is shown first, followed by the 3D color-maps of the maximum and minimum principal stresses that can be used in future works to examine the differences between simulation and experimental XRD investigations on printed part.

Figures 7.1 and 7.2 show the equivalent stress over the entire volume and, respectively, the locations of the maximum and minimum equivalent stress. The maximum value is experienced where the slots originate from the core, and thus can be explained in terms of geometrical stress concentration. Its value reaches more than 450 MPa in tension.

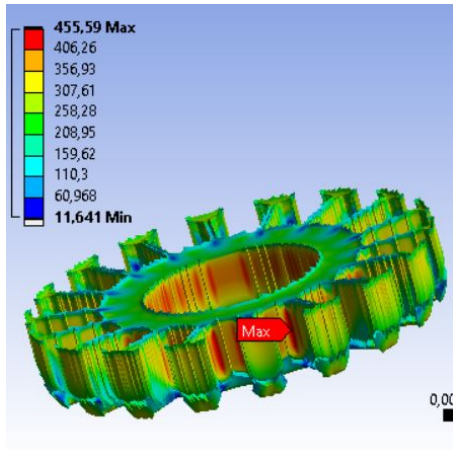


Figure 7.1: *Equivalent Stress; max location*

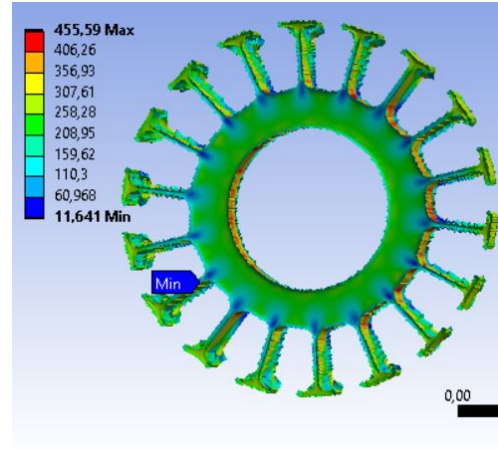


Figure 7.2: *Equivalent Stress; min location*

The plots for the maximum principal stress and the locations of the

minimum and maximum values are displayed in Figures 7.3 and 7.4. The maximum magnitude reaches almost 500 MPa in tension inside the slot, while the minimum value is a compressive stress that is experienced on the bottom of the rotor. The top surface resents a tensile stress with a magnitude of around 250 MPa. This result seems to agree with the theory of cool-down mechanism, in which the top layers experience a tensile bending stress while the bottom layers undergo compressive stress due to the difference in temperature and thermal contraction.

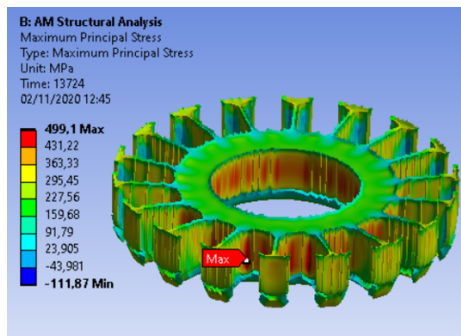


Figure 7.3: *Maximum principal stress; location of the maximum value*

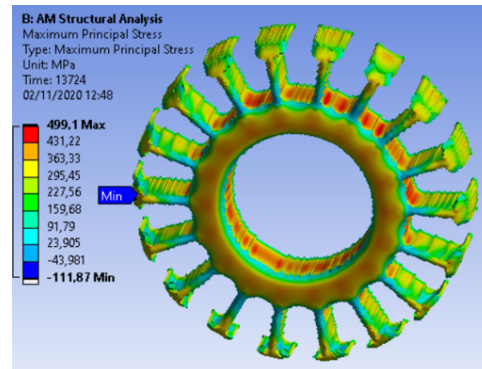


Figure 7.4: *Maximum principal stress; location of the minimum value*

The minimum principal stress over the entire volume is shown in Figure 7.5 below.

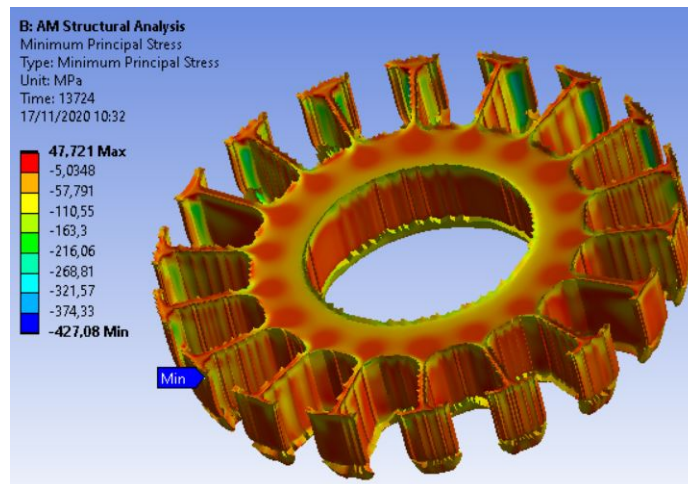


Figure 7.5: *Minimum Principal Stress*

The minimum value - a compressive stress of more than 400 MPa - is

experienced on the external vertical faces of the slot. Compression is also found in almost all the contour edges of the geometry, while the central areas of the volume resent low tensile stress ($< 50MPa$). This result can be described by the temperature gradient mechanism (TGM). As detailed in *Chapter 4*, the TGM theory illustrates the origin of compressive and tensile stress in different regions of the same layer because of the temperature difference between the melted track and the previous tracks of the same bed. This thoery is strictly related to the scanning strategy, which is not taken into account in AM ANSYS Workbench. Indeed, an axial symmetry is obtained in the resulting stress as a consequence of the geometry symmetry. This result is not completely accurate, because the difference in stress on an horizontal face is highly influenced by the scanning strategy. However, due to the temperature gradients and the difference in cooling rates, a faster cool-down is expected towards the edges, thus inducing compression state, while tensile stress is generated in the central area with bending occuring in the opposite direction to the energy source.

The total deflection resulting from the FE analysis is shown in Figure 7.6 with a scale of 10. The maximum value is slightly below 1 mm and it is encountered on the external vertical face of the slot, towards the bottom layers. This result can be explained in terms of the geometry detail of the slot but also becuae of the removal steps causing a stress relief, and thus distortion.

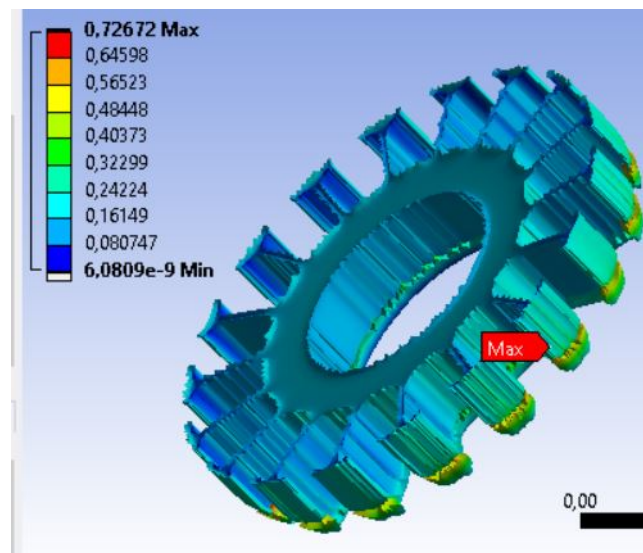


Figure 7.6: *Total deflection (scale 10)*

The above stress results were used to compare their trends with those

of previous studies as described hereafter.

A line was identified in the rotor volume, from the bottom layers to the top face. Its location is shown in Figure 7.7. This 1D geometry was used to plot the maximum principal stress, the minimum principal stress and the equivalent stress as a function of the building direction, from 0 mm to the total height of the rotor (16 mm). The graphs are illustrated in Figures 7.8, 7.9 and 7.10, respectively.

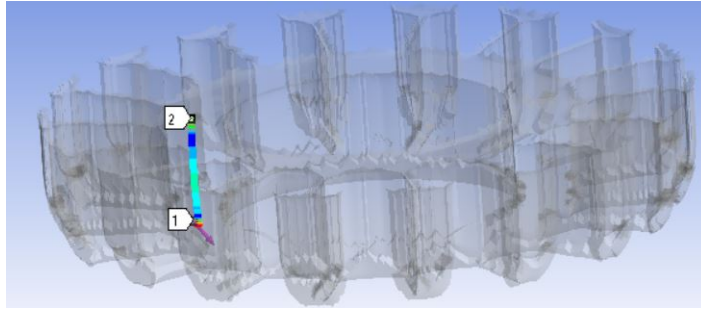


Figure 7.7: *Vertical line in the rotor volume*

The graphs show that there is a strong dependence on the z-coordinate, where the z-axis coincides with the building direction of the process. This result is in agreement with the findings of previous studies on residual stress in SLM, namely [59] and [61]. Those works investigated residual stress in SLM components via several methods, both numerical and experimental. The geometries were respectively a cube and a cantilever, but a variation with z-coordinate was found in those studies, too.

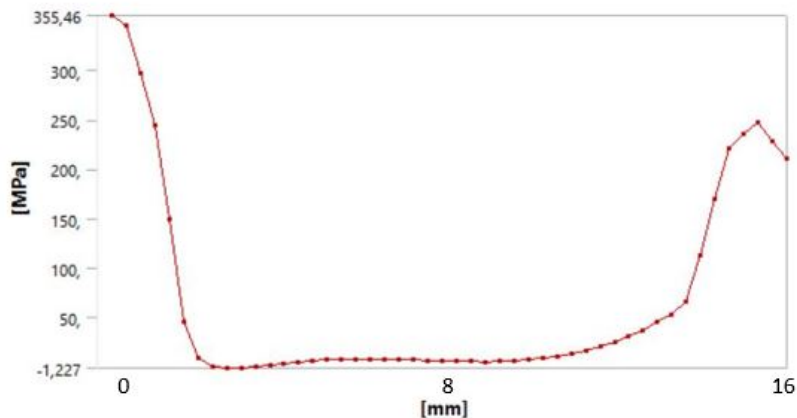


Figure 7.8: *Maximum Principal Stress as a function of z-coordinate (building direction)*

The bottom layers present a high tensile stress in the maximum principal direction, and a minimum principal stress that is very close to 0 MPa. The volume at intermediate values of z undergoes a compressive state, with the maximum principal stress being almost null and the minimum principal stress reaching just below -200 MPa. On the upper part, the stress state is similar to the bottom layers, but the maximum principal stress hitting a lower value and with a peak just below the top face.

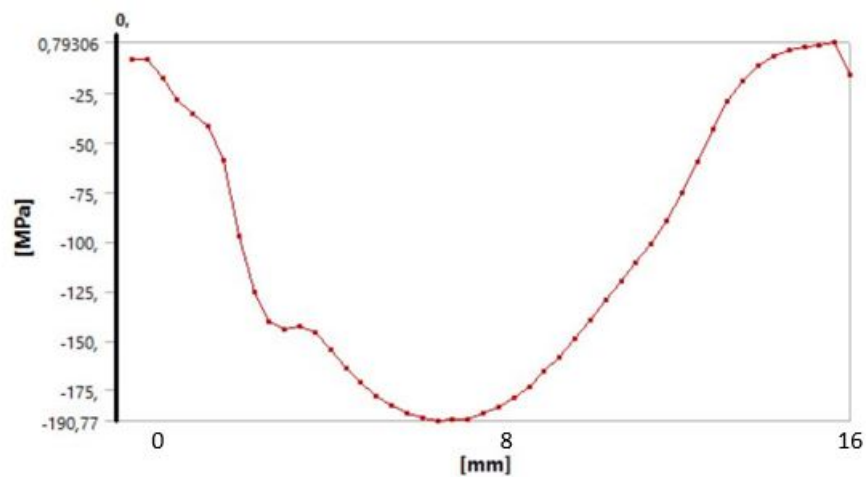


Figure 7.9: *Minimum Principal Stress as a function of z-coordinate*

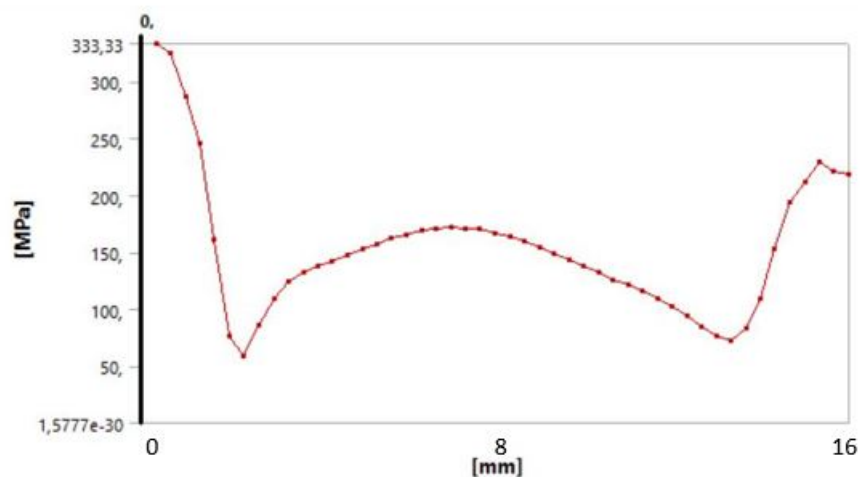


Figure 7.10: *Equivalent Stress as a function of z-coordinate*

7.1 Check of accuracy of the model

The residual stress and deflection discussed in the previous paragraph are the result of a convergence analysis that was performed by progressively refining the mesh. Since the target of the analysis is the rotor, no mesh refinement was performed on the build plate base where the mesh size was always kept at 5 mm. Instead, on the build part (the rotor) an initial size of 2 mm was used to run the first simulation and a threshold of 3% was assumed to consider the solution converged during the next steps.

The intermediate results during iterations are listed in the tables below (Table 7.1), together with the relative change between one step and the other (Table 7.2).

	Mesh size			
	2 mm	1 mm	0.8 mm	0.6 mm
Equivalent stress (MPa)	394.69	433.11	448.75	455.59
Max Principal stress (MPa)	433.64	457.07	483.75	499.1
Min Principal stress (MPa)	33.842	30.901	44.34	47.721
	-376.65	-408.86	-422.11	-427.08

Table 7.1: *Intermediate results of the convergence analysis*

Mesh size	Equivalent stress (MPa)	Relative change	Convergence check
2 mm	394.69	-	-
1 mm	433.11	+9.6%	> 3%
0.8 mm	448.75	+3.7%	> 3%
0.6 mm	455.59	+1.5%	< 3% OK

Table 7.2: *Relative change for convergence check*

The analysis was stopped at 0.6 mm since a change of 1.5% ($< 3\%$) is experienced in the residual stress with respect to the previous iteration. This is a positive result since the mesh size of 0.6 mm exceeds the layer thickness by one order of magnitude which is a mathematical/physical requirement. The graph resulting from the analysis (Figure 7.11) shows a relative increase in the equivalent stress by around 15% between the simulation performed with a mesh size of 2 mm and 0.6 mm, respectively. An horizontal asymptote can be drawn towards 460 MPa.

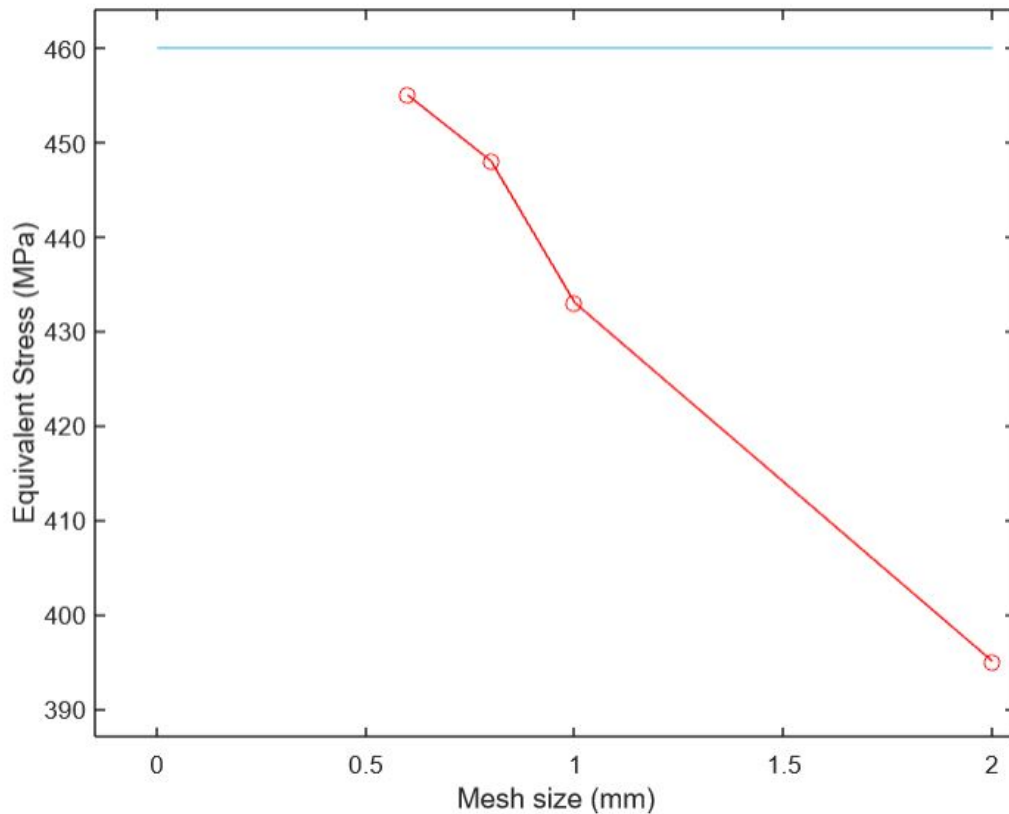


Figure 7.11: *Convergence analysis: equivalent stress versus mesh size*

The convergence analysis described in this paragraph may be considered as an initial examination of the accuracy of the model and its boundary conditions. The outcome of this part of the work is extremely encouraging from both a mathematical and physical standpoint. Indeed, the converged results show that the problem is mathematically well-posed; while the physical discussion of the stresses made previously in this chapter highlights the accordance with the theories explaining residual stress in SLM parts. However, it is strongly recommended for future work to compare the prediction of residual stress that is made in this study by FEA with experimental values.

7.2 Sensitivity analysis: energy density

Residual stress and the resulting distortion can lead to a reduction on mechanical performance and even cause the part to be unacceptable. Then, the mitigation strategies are investigated in this paragraph. The literature

review on SLM and residual stress points out that the following approaches can be followed to reduce the stress that remains in the part after its additive manufacture:

- tuning of process parameters;
- post-processing via heat treatments;
- change in desing.

Post-processing via heat treatments is not part of this work, since it would necessarily require experimental testing on printed part and its study cannot be conducted by numerical simulation. The influence of the geometry is another significant influencing factor in the residual stress magnitude. The part desing is taken into account in this work through a topological optimization, as described in the following chapter.

Instead, this paragraph will focus on the influence of process parameters and, in particular, energy density $E[J/mm^3]$. The energy density gives an indication of the average energy introduced during the exposure of a layer per material volume and it can be computed as:

$$E = \frac{P}{v_s * h * t}$$

where:

- P [W] is the laser power;
- v_s [mm/s] is the scanning speed;
- h [mm] is the hatch spacing;
- t [mm] is the layer thickness.

It can be noticed that the most charateristic process parameters are included in the definition of E , that is the focus of this part of the study. The first combination of process parameters is shown in the table below and is used as reference.

Reference Combination				
Laser Power [W]	Scan speed [mm/s]	Hatch spacing [mm]	Layer thickness [mm]	Energy density [J/mm^3]
90	800	0.07	0.03	53.57

Table 7.3: *Process parameters in the reference combination*

Since the laser power P was not an input in ANSYS AM Workbench analysis, a value of 90 W was assumed and kept constant in all the combinations, while the other factors were tuned to give different values of energy density, as shown in Table 7.4.

	Combination n.				
	1 (reference)	2	3	4	5
Laser power [W]	90	90	90	90	90
Scan speed [mm/s]	800	1500	700	600	400
Hatch spacing [mm]	0.07	0.09	0.06	0.05	0.05
Layer thickness [mm]	0.03	0.08	0.03	0.03	0.03
Energy density [J/mm^3]	53.6	8.3	71.4	100	150
Equivalent stress [MPa]	455.59	432.41	459.39	460.64	461.01

Table 7.4: Results of process parameter tuning mitigation strategy

As listed in the table, five combinations of parameters were tested giving five different values of energy density, namely $53.6 J/mm^3$ (reference value), $8.3 J/mm^3$, $71.4 J/mm^3$, $100 J/mm^3$, $150 J/mm^3$. The graph in Figure 7.12 shows that a reduction of residual stress is experienced with the set of parameters that results in the lowest energy density ($8.3 J/mm^3$). On the contrary, a slight increase is found when the energy density is doubled and tripled ($100 J/mm^3$, $150 J/mm^3$), while with $71.4 J/mm^3$ the difference in residual stress with the reference case ($53.6 J/mm^3$) seems to be non-significant. This finding is in agreement with previous works showing that the energy density does not influence the residual stress if its value is changed so that the resulting part is full-dense. Indeed, most probably the combination resulting in $71.4 J/mm^3$ of energy density still gives a dense component.

The variation of residual stress with the change of energy density was expected, however the outcome of this part of the work may indicate that tuning the process parameters is not the most effective mitigation strategy for the high residual stress in SLM produced components. Indeed, the mag-

nitude of the equivalent stress reduces by only less than 6% when the energy density is decreased from 53.6 J/mm^3 to 8.3 J/mm^3 . Such a low value of energy density would most probably result in a non-full dense part with void formations and internal cracks. A minimum energy density is required to completely melt the part, thus ensuring as less pores as possible. Instead, high energy densities not only do not guarantee a significant reduction in stress, but also they may be the cause of vaporization and key-hole effect.

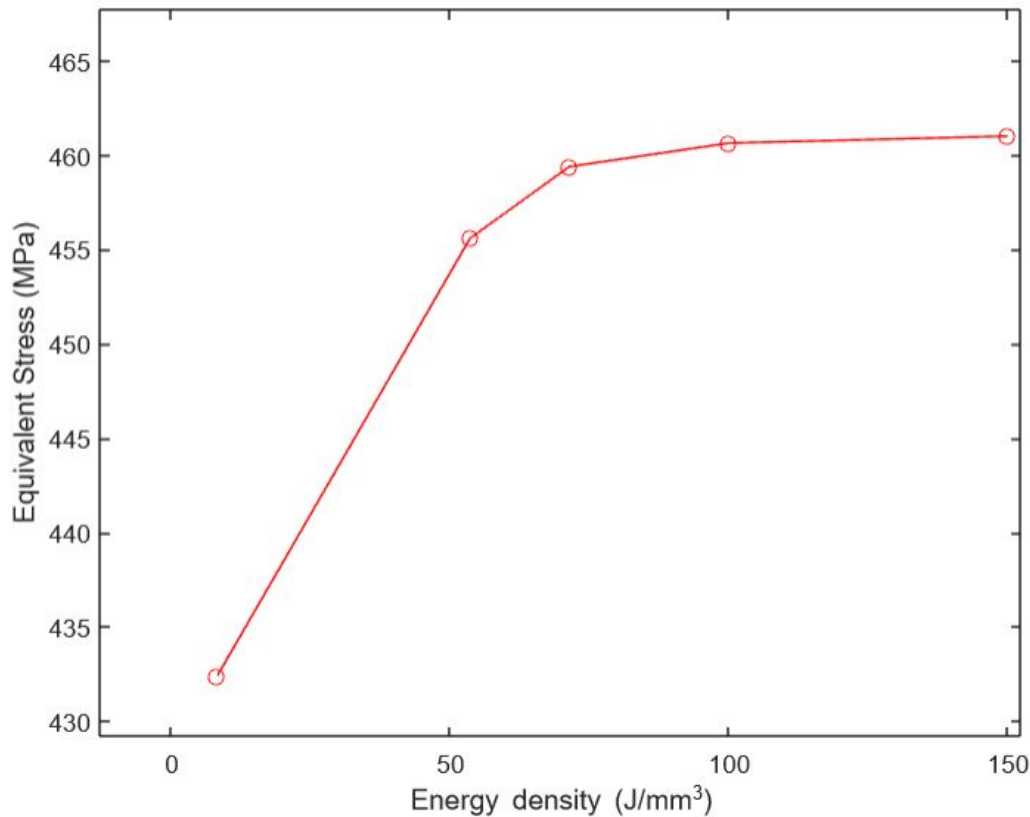


Figure 7.12: *Sensitivity analysis: equivalent stress versus energy density*

The primary goal when producing a part by SLM should be to find the optimal range for all the process parameters to guarantee an high density. Thus, it can be concluded that tuning the process parameters in their optimal range may not be enough to reduce the residual stress. Post-processing via heat treatments is certainly an alternative that is recommended for future investigations, since this is not part of this work.

Finally, it should be noted that some parameters cannot be controlled by ANSYS Workbench, but they may influence the residual stress, conse-

quently they may be adjusted with the objective of mitigating the stress. That is the case of the scanning strategy, whose examination is also recommended for future developments of this subject.

Chapter 8

Topological optimization

The last part of this work consists in a mechanical topological optimization of the rotor, as described in the current chapter. The dedicated ANSYS tool was used for this purpose. However, the ANSYS topology optimization tool does not work properly with non-linear materials and needs to be applied after a *static structural* box. Then, the following workflow was used to find a mechanically optimized geometry for the rotor:

- the reference rotor - described in *Chapter 6* - is used to run a structural analysis. A similar material is used instead of the AM material and a fictitious load is applied so that the equivalent stress is similar to what is found in the FE simulation of the AM process (*Chapter 7*);
- the outcome of this analysis is used as input of the topological optimization tool;
- the resulting geometry is saved and simplified in ANSYS SpaceClaim or any other 3D CAD software. In this step, the build base plate is also copied in the model, to create the assembly that is required in the AM process simulation;
- the assembly is used as geometrical input of an AM ANSYS analysis, where all the settings are the same as the reference case (*Chapter 7*).

The workflow to get the optimized shape is shown in figure 8.1.

It should be noted that the analysis was performed by taking into account only the mechanical loads with the objective of reducing the mass of the rotor without increasing the equivalent stress or total deflection in the part. The setting and results of this analysis are illustrated in the following paragraphs.

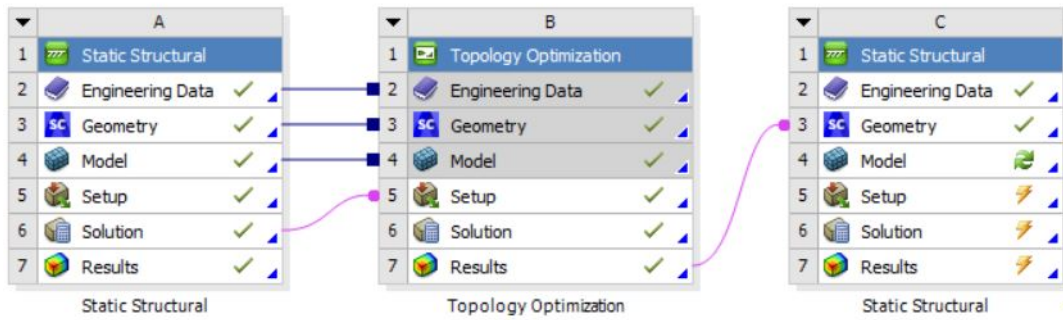


Figure 8.1: *Workflow for topological optimization of AM parts in ANSYS*

8.1 Settings of the topological optimization

The mechanical optimization of the rotor was aimed at proposing a lighter design of the part to benefit from one of the best advantages of AM processes, which is the quasi-total freedom in design. In this study, only the mechanical loads were considered as resulting from the AM thermal-to-structural analysis. Instead, no electromagnetic consideration was made, but the analysis of the electromagnetic properties of the optimized shape is highly recommended for future works, preferably on the printed part.

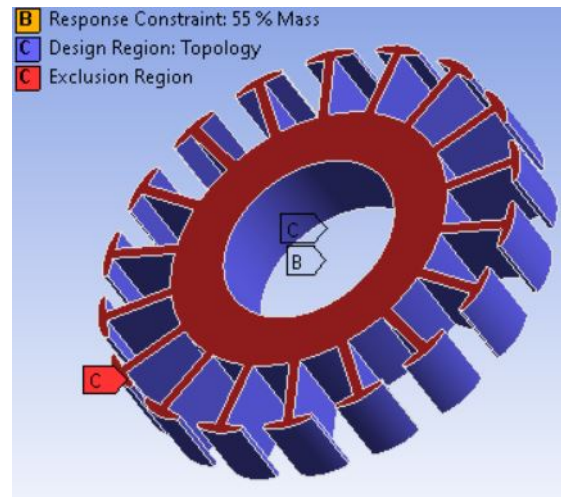


Figure 8.2: *Geometrical settings of the topological optimization analysis in ANSYS*

The geometrical settings of the analysis are shown in figure 8.2. Two main regions can be identified:

- a *topology region*, where the material can be removed;
- an *exclusion region*, where the material is kept for constraints/load application or for the coupling with other systems.

In the case of the AM production of a rotor, there is no need to consider faces or points to retain for the application of loads, but the external upper and lower faces were included in the exclusion region as part of the contour geometry. Also, in the analysis of the optimized design options, the shapes with an high percentage of mass removal in the internal cylindrical face were not considered to allow for the coupling with the shaft. An example of geometry that was excluded is shown in figure 8.3: this design was obtained by setting a mass reduction of about 50%. Such a percentage of mass removal induced a great volume decrease in the central area, thus making the coupling with the shaft difficult.

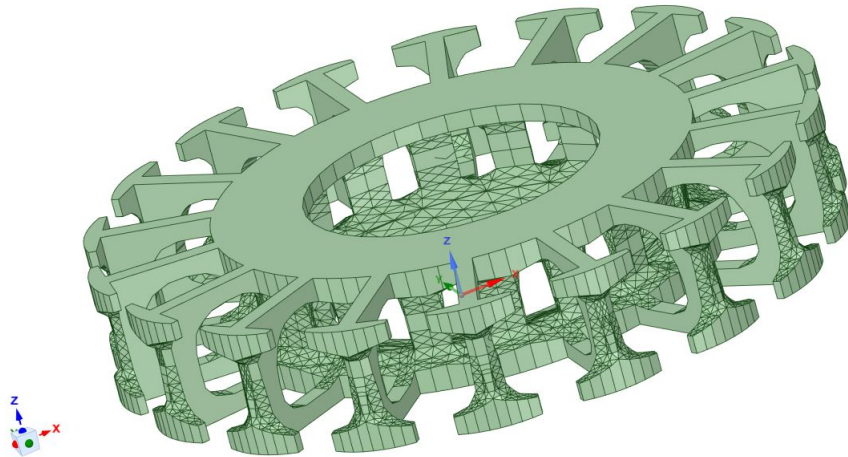


Figure 8.3: *Optimized geometry with 52% of mass retained*

8.2 Optimized proposed design

Based on the outcomes of the first optimization - having 52% of the initial mass in the final geometry -, lower percentages of reduction were tested subsequently. The geometries obtained with 70% and 60% of mass retained are illustrated in figures 8.4 and 8.5, respectively. They are both characterized by moderate mass removal in the internal cylindrical face, thus making the shape acceptable. In both cases a considerable mass reduction is experienced in the area of the slots and on the external cylindrical face

with a greater removal in case of 60% of mass remained in the final design. Then, they were both used to run an AM structural-to-thermal analysis and evaluate the equivalent stress and total deflection.

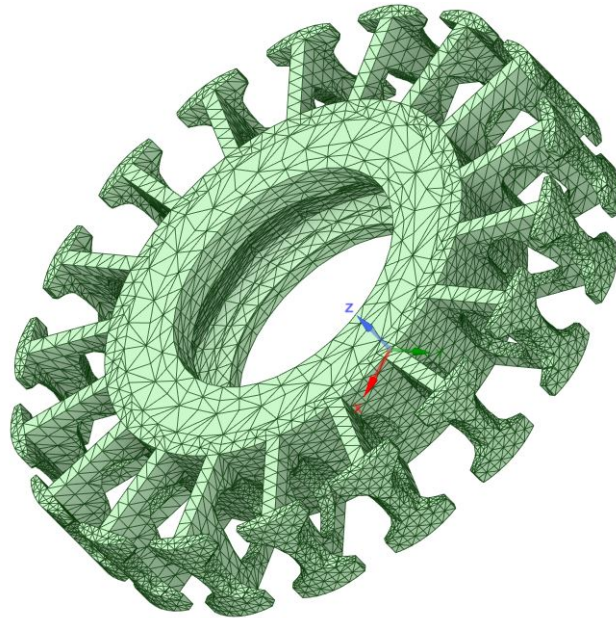


Figure 8.4: *Optimized geometry with 70% of mass retained*

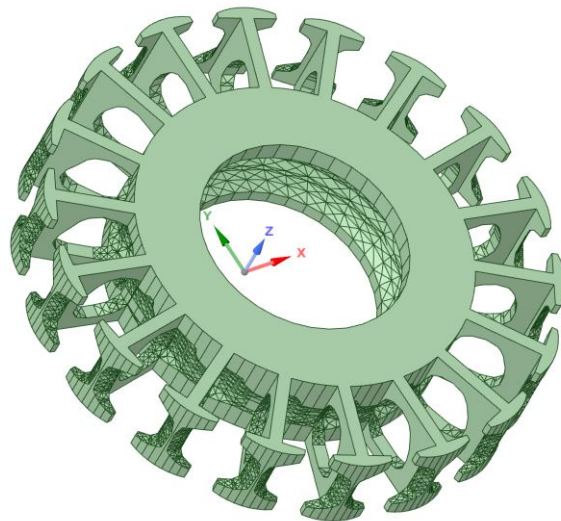


Figure 8.5: *Optimized geometry with 60% of mass retained*

The total deflection in the design with 70% of volume is shown in Figures 8.6 and 8.7 in the true scale and with a scale of 16:1, respectively. The maximum value is around 0.80 mm and is found to be on the external vertical face of the slot. A similar result was also found in the reference - non-optimized - design. The reason for this finding is most probably linked to the geometry detail of the slot location and its consequent stress concentration. The invariance of the total deflection was one of the target of the topological analysis, thus making this design admissible.

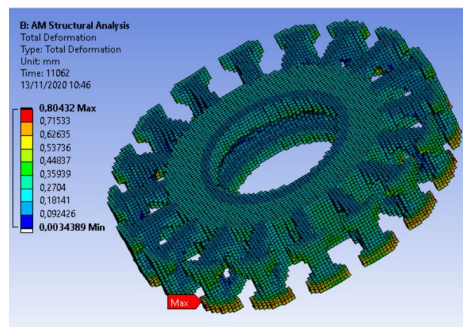


Figure 8.6: *Design with 70% mass retained. Total deflection - true scale*

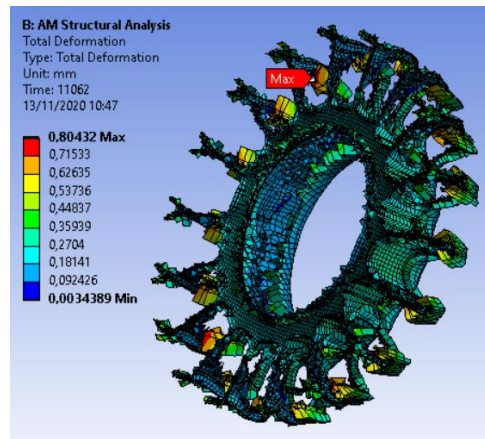


Figure 8.7: *Design with 70% mass retained. Total deflection - scale 16*

The equivalent stress was also evaluated in the optimized shape with respect to the reference case. It was found that the location of the maximum equivalent stress is still experienced inside the slot site. However, the magnitude is slightly lower (423 MPa instead of 455 MPa). This second result also makes the current design eligible as a lighter geometry for further investigations. Finally, one last design was studied, as detailed hereafter. A percentage between 52% and 70% of mass retained was chosen for the last trial.

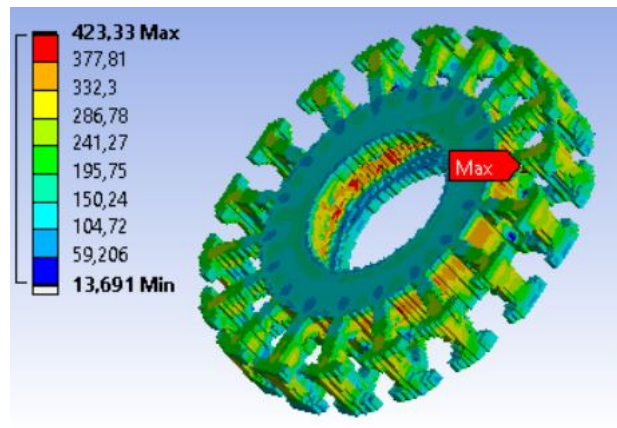


Figure 8.8: *Design with 70% mass retained. Equivalent stress - true scale*

The last optimized design was characterized by a final volume being 60% of the initial one. The total deflection was found to be around the same value as the previous cases (0.80 mm) as shown in both true and modified scale (Figures 8.9 and 8.10).

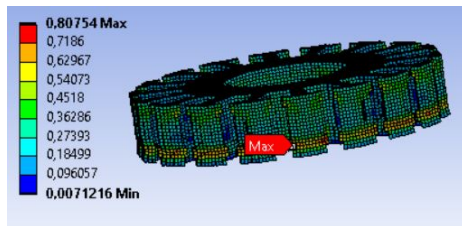


Figure 8.9: *Design with 60% mass retained. Total deflection - true scale*

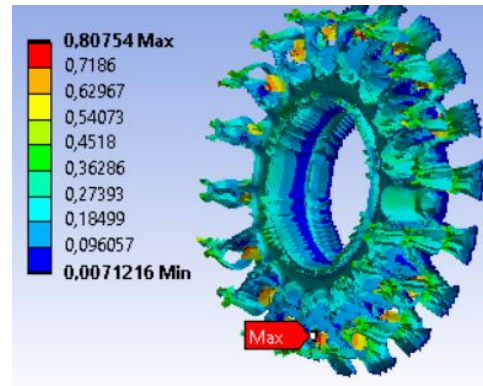


Figure 8.10: *Design with 60% mass retained. Total deflection - scale 16*

The equivalent stress with a design being 40% lighter was found to be lower than both the reference case (non-optimized) and the previous optimized case (30% lighter than reference). The location of the maximum is still the same, in the internal part of the slot. The values of the equivalent stress and total deflection make this design admissible, too. This case is certainly preferable in terms of weight, however more examination may be required to decide the optimal shape. A summarizing table illustrates the outcomes of the mechanical topological analysis (Table 8.1).

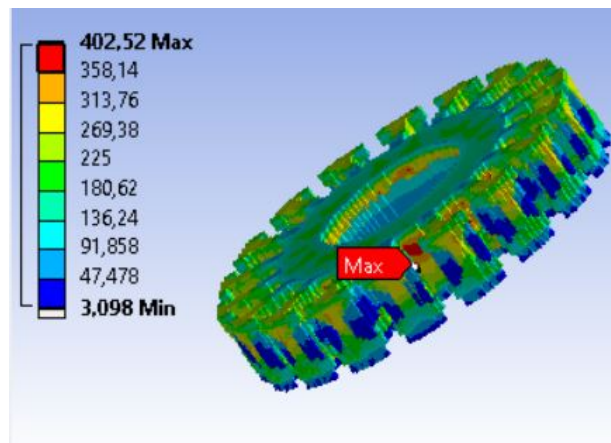


Figure 8.11: *Design with 60% mass retained. Equivalent stress - true scale*

Topological optimization iterations				
Steps	Retained mass	Total deflection [mm]	Equivalent Stress [MPa]	Comments
STEP 1	52%	-	-	non acceptable
STEP 2	70%	0.8043	423.33	acceptable
STEP 3	60%	0.8075	402.52	acceptable

Table 8.1: *Retained mass, total deflection and equivalent stress during topological optimization*

The topological optimization analysis was performed by trial and error. Three different weight reduction were studied with the following results:

- a design with 48% of volume removal was obtained as first attempt: its shape was considered non-acceptable for the amount of mass removal in the central area, where the rotor is coupled to the shaft;
- a second trial was done by removing 30% of mass from the initial design: total deflection did not change while the equivalent stress decreased slightly;
- a last trial was run with a 40% mass reduction: the simulation results were almost the same as the second trial but with an even lower equivalent stress.

Based on those results, both the second and the third designs are acceptable. The lighter between them (40% of mass removed) is preferable because of both the weight and the low stress. However, for a complete validation of an optimized rotor, it is recommended to physically print the component to also test its electromagnetic performances. The encouraging result of this part of the study is the demonstration that optimized electric rotor can be obtained by SLM without increasing the residual stress (and its consequent distortion) that is inherent in the SLM process.

Chapter 9

Conclusions and final remarks

The extensive review of the state of the art about AM applied to electrical machines demonstrated that AM can be an alternative to the conventional way of producing electrical machines and, even more, it can address the high-demanding requisites of this field in terms of sustainability and economic growth. As yet, disparate studies showed how promising AM may be in reducing printing operations, postprocessing steps, wasted materials [20] and in producing lightweight components, but some steps are still needed before an AM electric motor can be commercialized.

One of the hurdle consists in searching for the optimal settings of the process to guarantee both a full-dense component and the desired electromagnetic properties. Some previous research evaluated how the process can be tuned to get a part having the same mechanical properties as the bulk material, but with poor electromagnetic properties. Based on the few 3D-printed cores in literature, multimaterial techniques may be the key for the developments of AM electric motors, as pointed out by the authors of [1]. The simultaneous use of different materials may help in reaching all the desired properties: for instance, electrical steel and magnetic insulators may reduce the eddy current losses [1][20].

The research in this field are currently based on design of experiments and consequent expensive printings of numerous samples to be physically tested. An important improvement to make the investigations faster and less expensive may be the use of simulation tools to predict the microstructure and properties of the AM-produced electric machines with almost no waste of material.

This thesis work proved how finite element analysis may be applied in the early stages of the research in place of physical printings. In particular, FE simulation was used in this study to predict the residual stress, which

is an inherent defect of AM that needs to be considered during design. The outcomes of the analysis seem to be in agreement with the models describing residual stress formation in SLM parts, namely TGM and cool-down mechanism. The stresses in the entire volume were investigated after the building and removal steps. A vertical line - parallel to the building direction - was used to explore the variation of residual stress with z-level. It was found that both the bottom layers and the upper part resent an high tensile stress (around 400 MPa) in the maximum principal direction, while the minimum principal stress was very close to 0 MPa. The opposite result was experienced at the intermediate values of z, with the maximum principal stress being almost null and the minimum principal stress reaching just below -200 MPa. Another encouraging result derives from the convergence analysis. The analysis was conducted by progressively refining the mesh with a target relative change of 3%. With a mesh size of 0.6 mm, the relative change was found to be 1.5%, thus allowing to stop iterating. The convergence analysis demonstrated that the problem is mathematically well-posed and may be seen as a first check of the accuracy of the model.

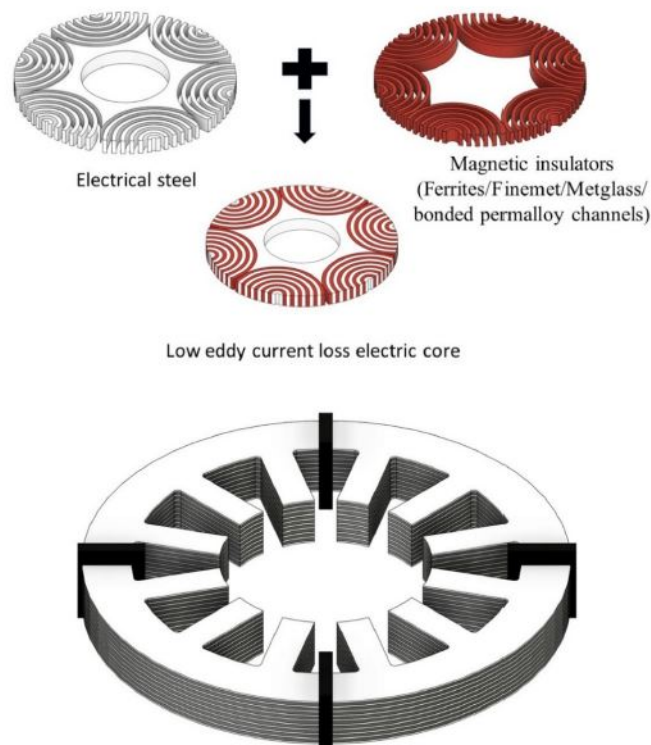


Figure 9.1: *Example of multimaterial design with alternating vertical sheets of electrical steel and magnetic insulator [20]*

A second section of the work consisted in a sensitivity analysis: the value of energy density was changed by tuning the process parameters. The consequent residual stresses were analysed to assess the effectiveness of adjusting the parameters in mitigating residual stress. The magnitude of the equivalent stress reduced by only 6% when the energy density was decreased from the reference value to 8.3 J/mm^3 . This value of energy density would most probably give a non-full dense part with void formations and internal cracks. Instead, a slight increase in residual stress was encountered when the energy density was doubled or tripled, while no significant variation is experienced when the energy density was increased by one-third, going from 54 J/mm^3 to 71 J/mm^3 . This latter finding was in agreement with previous works showing that the energy density does not influence the residual stress if its value is changed in a range that still gives full-dense parts. This section of the work can lead to the conclusion that tuning the process parameters is not the most effective mitigation strategy for the high residual stress in SLM produced components. Thus, other strategies should be investigated in further developments of this topic.

The last part of this thesis work involved a topological optimization of the rotor, based on the structural analysis of the part during its SLM production. The proposed design is obtained through trial and error by progressively decreasing the percentage of retained mass. The equivalent stress and the total deflection were checked at every iteration to verify that their levels did not exceed the maximum values found in the reference configuration. The geometry was also evaluated to exclude those designs having too much mass removal in the central area, where the coupling with the shaft happens. A mechanically optimized geometry was presented at the end of this study. It was characterized by a final mass being around 40% lighter than the initial rotor, while its deflection and equivalent stress did not increase.

From the literature review and numerical simulation, some important conclusions can be derived at the end of this work:

- Large-scale AM-production of electric machines is a priority target for the future of technology because of their application in many sectors. The promising results of the early studies justify further research and investment on this area to reach the adequate maturity of the technique.
- The FEA can be an alternative to the physical printing during the early stages of an electric motor study. Its application may help

choosing the process parameters to evaluate the resulting mechanical properties. The simulation in this work demonstrated the accordance between FEA and theoretical explanation of residual stress in SLM. However, it is recommended to compare FEA results with the outcomes of experimental tests.

- The findings of the sensitivity analysis suggest searching for more effective mitigation strategies for residual stress. For instance, studying the effects of heat treatments, pre-heating of both powder and build base is recommended for further investigations of this subject. The evaluation of the scanning strategy is also designated for future works, since its study was not possible in the commercial software used in this work.
- The lightweight geometry proposed at the end of the topological optimization analysis was studied from the mechanical standpoint. Its electromagnetic validation is left to future works.

Bibliography

- [1] Mostafa Yakout, M.A. Elbestawi, Liping Wang, Richard Muizelaar. *Selective laser melting of soft magnetic alloys for automotive applications*. By: The 6th Joint Special Interest Group meeting between euspen and ASPE: Advancing Precision in Additive Manufacturing; Nantes, France. 2019
- [2] Lindroos T., Riipinen T., Metsä-Kortelainen S., Pippuri J., Lagerbom J., Revuelta A., Metsäjoki J. *Soft magnetic alloys for selective laser melting*. By: EuroPM 2017 Congress and Exhibition; Milan, Italy. 2017
- [3] Martín F., García C., de-Tiedra P., Blanco Y., Aparicio M. L. *Sensitization of Powder Metallurgy Type 430L Stainless Steel Sintered in Nitrogen-Hydrogen Atmosphere*. In: Corrosion; 64: 70-82. 2008
- [4] Carreño-Morelli E., Rodriguez-Arbaizar M., Girard H., Hussein H., Herzog R. *Fe_{2.7}Si, Fe₅₀Ni and Fe₅₀Co Soft Ferromagnetic Materials by Powder Injection Moulding*. By: Powder Metallurgy World Congress PM2012; Yokohama, Japan. 2012
- [5] Yang Z et al. *Structures and magnetic properties of iron silicide from adaptive genetic algorithm and first-principles calculations*. In: Journal of Applied Physics; 124 073901. 2018
- [6] Zhang Y., Zhang M., Li D., Zuo T., Zhou K., Gao M. C., Sun B., Shen T. *Compositional Design of Soft Magnetic High Entropy Alloys by Minimizing Magnetostriction Coefficient in (Fe_{0.3}Co_{0.5}Ni_{0.2})_{100-x}(Al_{1/3}Si_{2/3})_x System*. In: Metals 99382. 2019
- [7] Sundar R. S., Deevi S. C. *Soft magnetic FeCo alloys: alloy development, processing, and properties*. In: International Materials Reviews; 50, 157-192. 2005
- [8] DebRoy T. et al. *Additive manufacturing of metallic components – Process, structure and properties*. In: Progress in Materials Science; 92, 112-224. 2018

- [9] Shifeng W., Shuai L., Qingsong W., Yan C., Sheng Z., Yusheng S. *Effect of molten pool boundaries on the mechanical properties of selective laser melting parts*. In: Journal of Materials Processing Technology; 214, 2660-2667. 2014
- [10] Thompson M. K. et al. *Design for Additive Manufacturing: Trends, opportunities, considerations, and constraints*. In: CIRP Annals; 65, 737-760. 2016
- [11] Yakout M., Cadamuro A., Elbestawi M. A. Veldhuis S. C. *The selection of process parameters in additive manufacturing for aerospace alloys*. In: The International Journal of Advanced Manufacturing Technology; 92, 2081-2098. 2017
- [12] Wang D., Dou W. and Yang Y. *Research on Selective Laser Melting of Ti6Al4V: Surface Morphologies, Optimized Processing Zone, and Ductility Improvement Mechanism*. In: Metals; 8 471. 2018
- [13] Van Hooreweder B. and Kruth J-P. *Advanced fatigue analysis of metal lattice structures produced by Selective Laser Melting*. In: CIRP Annals; 66, 221-224. 2017
- [14] Wu B., Pan Z., Ding D., Cuiuri D., Li H., Xu J. and Norrish J. *A review of the wire arc additive manufacturing of metals: properties, defects and quality improvement*. In: Journal of Manufacturing Processes; 35, 127-139. 2018
- [15] Yakout M., Elbestawi M. A. and Veldhuis S. C. *Density and mechanical properties in selective laser melting of Invar 36 and stainless steel 316L*. In: Journal of Materials Processing Technology; 266, 397-420. 2019
- [16] Yakout M., Elbestawi M. A. and Veldhuis S. C. *A study of thermal expansion coefficients and microstructure during selective laser melting of Invar 36 and stainless steel 316L*. In: Additive Manufacturing; 24, 405-418. 2018
- [17] Liverani E., Toschi S., Ceschini L. and Fortunato A. *Effect of selective laser melting (SLM) process parameters on microstructure and mechanical properties of 316L austenitic stainless steel*. In: Journal of Materials Processing Technology; 249, 255-263. 2017
- [18] Yakout M., Elbestawi M. A. and Veldhuis S. C. *On the characterization of stainless steel 316L parts produced by selective laser melting*. In: The International Journal of Advanced Manufacturing Technology; 95, 1953-1974. 2018

- [19] Pal S., Lojen G., Kokol V. and Drstvensek I. *Evolution of metallurgical properties of Ti-6Al-4V alloy fabricated in different energy densities in the Selective Laser Melting technique*. In: Journal of Manufacturing Processes; 35, 538-546. 2018
- [20] T.N. Lamichhane, L. Sethuraman, A. Dalagan, H. Wang, J. Keller, M.P. Paranthaman *Additive manufacturing of soft magnets for electrical machines- A Review*. In: Materials Today Physics (15). 2020
- [21] K. Rajaguru, T. Karthikeyan, V. Vijayan. *Additive manufacturing – State of art*. In: Materials Today: proceedings. 2019
- [22] Caiying Shen, Peng Shan, and Tao Gao. *A Comprehensive Overview of Hybrid Electric Vehicles*. In: International Journal of Vehicular Technology. 2011
- [23] Hadler J. *Aachener Kolloquium Fahrzeug und Motorentechnik*. 2009
- [24] *Encyclopedia Britannica*; Metallurgy: Permalloy. <https://www.britannica.com/technology/Permalloy> (accessed Dec. 18, 2019)
- [25] H. Shokrollahi, K. Janghorban. *Soft magnetic composite materials (SMCs)*. In: Journal of Material Processing Technologies; 189, 1-12. 2007
- [26] ASTM F2792 – 10 *Standard Terminology for Additive Manufacturing Technologies*.
- [27] Cassidy Silbernagel, Ian Ashcroft, Phill Dickens, Michael Galea. *Electrical resistivity of additively manufactured AlSi10Mg for use in electric motors*. In: Additive Manufacturing; 21, 395-403. 2018
- [28] Sunil C. Joshi and Abdullah A. Sheikh. *3D printing in aerospace and its long-term sustainability*. In: Virtual and Physical Prototyping; 10, 175-185. 2015
- [29] Jiun-Yu Lai. *A Study of the Fabrication of Thin Lamination Stator Cores by the Uniform Droplet Spray Process*. Master's Thesis at Massachusetts Institute of Technology. 1997
- [30] Rong Yang. *Electrified vehicle traction machine design with manufacturing considerations*. PhD Thesis at McMaster University (Mechanical Engineering). 2016

- [31] T. Wakisaka, Y. Kurosaki, S. Arai. *Electrical Steel Sheet for Traction Motor of Hybrid/Electrical Vehicles*, vol. 103, p. 5. 2013
- [32] C. Y. Yap, C. K. Chua, Z. L. Dong, Z. H. Liu, D. Q. Zhang, L. E. Loh, and S. L. Sing. *Review of selective laser melting: Materials and applications*. In: Applied Physics Review; 2. 2015
- [33] Zhichao Dong, Yabo Liu, Weibin Wen, Jingran Ge, and Jun Liang. *Effect of Hatch Spacing on Melt Pool and As-built Quality During Selective Laser Melting of Stainless Steel: Modeling and Experimental Approaches*. In: Materials (Basel). 2018
- [34] Efrain Aguilera, Jorge Ramos, David Espalin, Fernando Cedillos, Dan Muse, Ryan Wicker, Eric MacDonald. *3D Printing of Electro Mechanical Systems*. 2013
- [35] <https://en.engineering-solutions.ru/motorcontrol/motor/>
- [36] <https://www.tlclam.net/electric-motor-types/>
- [37] Detchko Pavlov. *Invention and Development of the Leade-Acid Battery*. In: Lead-Acid Batteries: Science and Technology Edition; Second Chapter. 2017
- [38] U. Kohler, In: J. Garche (Editor-in-chief), *Encyclopedia of Electrochemical Power Sources*, vol. 1, Elsevier, 2009, p. 271.
- [39] Mohammed Azher Therib. *Three Phase Induction Motors*. 2017
- [40] Yannis L. Karnavas, Ioannis D. Chasiotis, Emmanouil D. Peponakis. *Optimization of Standard PMDC Motors used in Automotive Applications for Higher Power Density*. By: Third International Conference on Mathematics and Computers in Sciences and in Industry (MCSI). 2016
- [41] Ning Ding, K. Prasad and T.T. Lie. *The electric vehicle: a review*. By Int. J. Electric and Hybrid Vehicles, Vol. 9, No. 1, 2017
- [42] IOMVM - *International Organization of Motor Vehicle*
- [43] Sara Giganto, Pablo Zapico, M. Ángeles Castro-Sastre, Susana Martínez-Pellitero, Paola Leo, Patrizia Perulli. *Influence of the scanning strategy parameters upon the quality of the SLM parts*. By: 8th Manufacturing Engineering Society International Conference. 2019

- [44] Pavel Hanzl, Miroslav Zetek, Tomáš Bakša, Tomáš Kroupa. The Influence of Processing Parameters on the Mechanical Properties of SLM Parts. By: 25th DAAAM International Symposium on Intelligent Manufacturing and Automation, DAAAM. 2014
- [45] Shigang Bai, Nataliya Perevoshchikova, Yu Sha and Xinhua Wu. *The Effects of Selective Laser Melting Process Parameters on Relative Density of the AlSi10Mg Parts and Suitable Procedures of the Archimedes Method*. In: Materials Science & Engineering. 2019
- [46] R. Rashid, S.H. Masood, D. Ruan, S. Palanisamy, R.A. Rahman Rashid, M. Brandt. *Effect of scan strategy on density and metallurgical properties of 17-4PH parts printed by Selective Laser Melting (SLM)*. In: Journal of Materials Processing Technology. 2017
- [47] Hengfeng Gu, Haijun Gong, Deepankar Pal, Khalid Rafi, Thomas Starr, Brent Stucker. *Influences of Energy Density on Porosity and Microstructure of Selective Laser Melted 17-4PH Stainless Steel*. By: 24th Annual International Solid Freeform Fabrication Symposium. 2013
- [48] I. Yadroitsev, Ph. Bertrand, I. Smurov. *Parametric analysis of the selective laser melting process*. In: Applied Surface Science 253(19):8064–8069. 2007
- [49] B. Barroqueiro, A. Andrade-Campos, R. A. F. Valente and V. Neto. *Metal Additive Manufacturing Cycle in Aerospace Industry: A Comprehensive Review*. In: Journal of Manufacturing and Materials Processing. 2019
- [50] Martin B. Bezuidenhout, DimitarM. Dimitrov, Anton D. van Staden, Gert A. Oosthuizen, and LeonM. T. Dicks. *Titanium-Based Hip Stems with Drug Delivery Functionality through Additive Manufacturing*. In: BioMed Research International 2015(4):1-11. 2015
- [51] John. A. Slotwinski, Edward J. Garboczi, and Keith M. Hebenstreit. *Porosity Measurements and Analysis for Metal Additive Manufacturing Process Control*. In: Journal of Research of the National Institute of Standards and Technology. 2014
- [52] M. Wirth, F. Thiesse. *Shapeways and the 3D printing revolution*. By: European Conference of Information Systems; Tel-Aviv, Israel. 2014
- [53] A. Gebhardt. *Understanding Additive Manufacturing*. 2012

- [54] Jingchao Jiang, Xun Xu and Jonathan Stringer. *Support Structures for Additive Manufacturing: A Review*. In: Journal of Manufacturing and Materials Processing; 2. 2018
- [55] C.C. Chan. *The state of the Art of Electric and Hybrid Vehicles*. In: Proceedings of the IEEE, vol. 90, no. 2. 2002
- [56] Thomas Simsona, Andreas Emmela, Anja Dwarsb, Juliane Bohmb. *Residual stress measurements on AISI 316L samples manufactured by selective laser melting*. In: Additive Manufacturing. 2017
- [57] Peter Mercelis and Jean-Pierre Kruth. *Residual stresses in selective laser sintering and selective laser melting*. In: Rapid Prototyping Journal. 2006
- [58] R. Acevedo, P. Sedlak, R. Kolman, M. Fredel. *Residual stress analysis of additive manufacturing of metallic parts using ultrasonic waves: State of the art review*. In: Journal of Material Research and technology; 9(4), 9457-9477. 2020
- [59] Jenni Pippuri, Sini Metsä-Kortelainen, Tomi Lindroos, Mikko Savolainen, Antero Jokinen, Alejandro Revuelta, Antti Pasanen, Kimmo Ruusuvoori. *3D printing of soft magnetic cores for electrical machines*. By: Proceedings of the 1st Annual SMACC Research Seminar. 2016
- [60] M. Yakout and M. A. Elbestawi. *Residual Stress Formation in Laser-Based Powder Bed Fusion (PBF-LB) of Invar 36*. In: Structural Integrity of Additive Manufactured Materials and Parts, ed. N. Shamsaei and M. Seifi (West Conshohocken, PA: ASTM International, 2020), 34–44.
- [61] Riipinen T., Metsä-Kortelainen S., Lindroos T., Keränen J. S., Manninen A., Pippuri-Mäkeläinen J. *Properties of soft magnetic Fe-Co-V alloy produced by laser powder bed fusion*. In: Rapid Prototyping Journal. 2019
- [62] <https://grabcad.com/>